

RESEARCH

Open Access



Microstructural and petrophysical properties of the Permo-Triassic sandstones (Buntsandstein) from the Soultz-sous-Forêts geothermal site (France)

Michael J. Heap^{1*}, Alexandra R. L. Kushnir¹, H. Albert Gilg², Fabian B. Wadsworth³, Thierry Reuschlé¹ and Patrick Baud¹

*Correspondence:

heap@unistra.fr

¹ Géophysique

Expérimentale, Institut de Physique de Globe de Strasbourg (UMR 7516, CNRS, Université de Strasbourg/EOST), 5 rue René Descartes, 67084 Strasbourg Cedex, France

Full list of author information is available at the end of the article

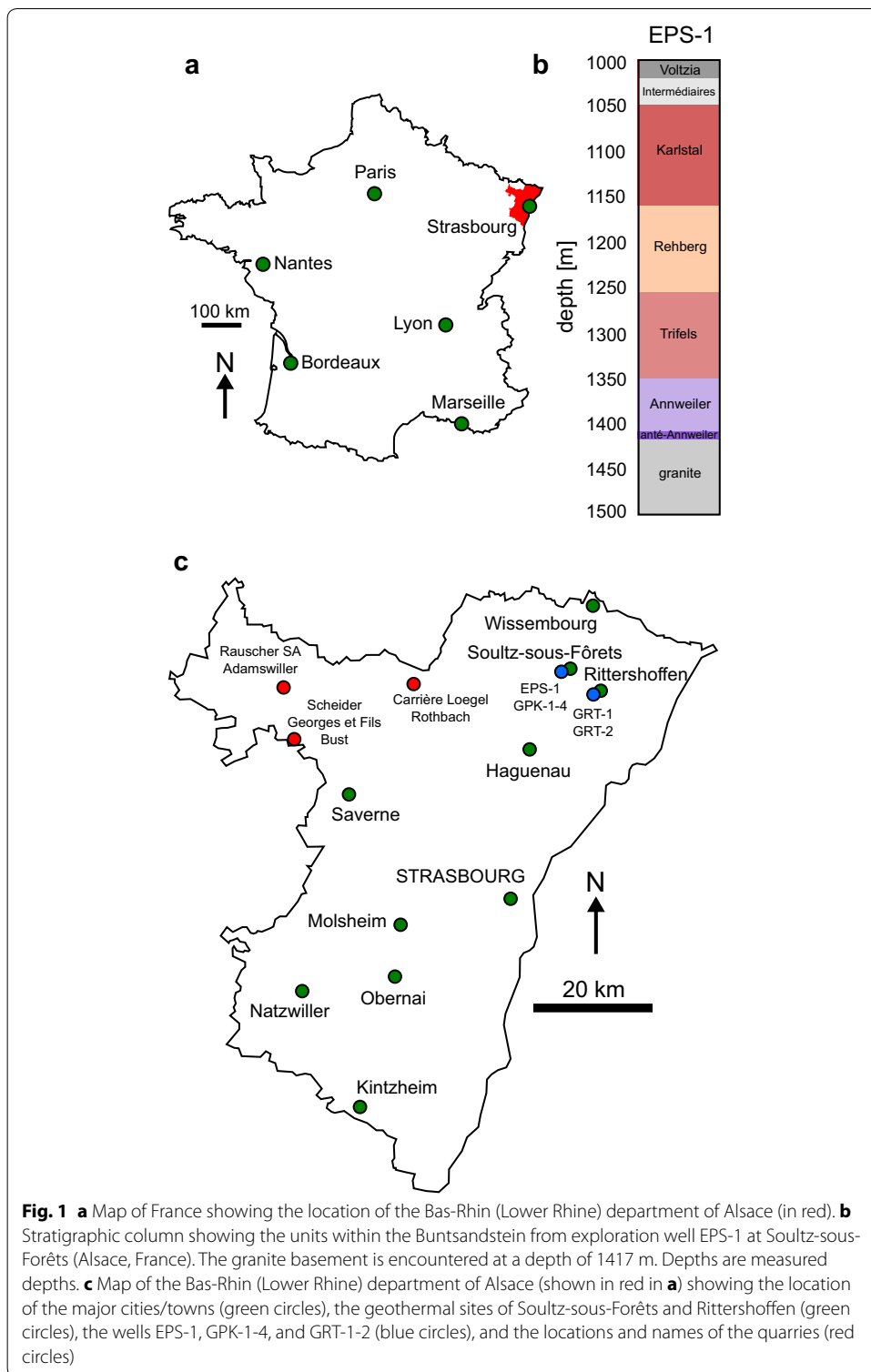
Abstract

Geothermal projects in the Upper Rhine Graben aim to harness thermal anomalies that have arisen due to hydrothermal circulation within the granitic basement and the overlying Permo-Triassic sedimentary units. We present here a systematic microstructural, mineralogical, and petrophysical characterisation of the lowermost unit of this Permo-Triassic sedimentary succession—the Buntsandstein—sampled from exploration well EPS-1 at the Soultz-sous-Forêts geothermal site (France). Twelve depths were sampled (from 1008 to 1414 m) and cylindrical cores were prepared perpendicular and parallel to bedding. These cores were described in terms of their microstructure, grain size and shape, specific surface area, pore size and pore throat size distribution, mineral content, porosity, *P*-wave velocity, and permeability. The Buntsandstein sandstones are predominantly feldspathic sandstones, often characterised by pores filled or partially filled (with clays (R3 illite–smectite), dolomite, siderite, and barite) as a consequence of diagenesis, tectonics, and the circulation of hydrothermal fluids. The porosity, dry *P*-wave velocity, and permeability of these sandstones vary from ~ 0.03 to 0.2, ~ 2.5 to 4.5 km s⁻¹, and ~ 10⁻¹⁸ to 10⁻¹³ m², respectively. Our data show that *P*-wave velocity decreases and permeability increases as porosity increases. *P*-wave velocities are significantly higher when measured parallel to bedding (by about 10 to 25%), and that saturation with water increases *P*-wave velocity (by about 5 to 50%, depending on sample orientation). The pervasive pore-filling precipitation has significantly reduced the permeabilities of the Buntsandstein sandstones, which are orders of magnitude less permeable than similarly porous unaltered sandstone. We also find that their permeability can be up to an order of magnitude more permeable when measured parallel to bedding than perpendicular to bedding. Although Buntsandstein units with low matrix permeabilities (as low as ~ 10⁻¹⁸ m²) require macroscopic fractures to attain the high permeability required to sustain regional hydrothermal circulation, matrix permeability is important for units with low fracture densities and high matrix permeabilities. We anticipate that these data will aid future fluid flow modelling and seismic investigations at geothermal sites within the Upper Rhine Graben.

Background

Thermal anomalies (~ 100 °C/km) in the Upper Rhine Graben—a rift valley that straddles the border between eastern France and western Germany—are attributed to hydrothermal circulation within the fractured Palaeozoic granitic basement and the overlying Permian and Triassic sedimentary units (e.g. Pribnow and Schellschmidt 2000; Buchmann and Connolly 2007; Guillou-Frottier et al. 2013; Baillieux et al. 2013; Magnenet et al. 2014). The granitic basement, and the interface between the Permo-Triassic sedimentary units and the granite, has consequently received considerable attention for geothermal energy exploitation. Notable examples include the enhanced geothermal system (EGS) sites at Soultz-sous-Forêts (France) (e.g. Gérard and Kappelmeyer 1987; Kappelmeyer et al. 1991; Baria et al. 1999; Gérard et al. 2006), Rittershoffen (France) (e.g. Baujard et al. 2017), Brühl (Germany), Landau (Germany), Insheim (Germany), Bruchsal (Germany), and Riehen (Switzerland). Two sites are currently in development close to Strasbourg, in Illkirch and Vendenheim (both in France). Despite the importance of the Permo-Triassic sedimentary units (namely the Buntsandstein, the Muschelkalk, and the Keuper; Aichholzer et al. 2016) for regional hydrothermal convection (e.g. Ledésert et al. 1996; Aquilina et al. 1997) and as a heat-exchanger, the majority of studies aimed at assessing or quantifying the permeability at the geothermal sites at Soultz-sous-Forêts and Rittershoffen, for example, have focussed on the granite basement (e.g. Genter and Traineau 1996; Shapiro et al. 1999; Sausse et al. 2006; Dezayes et al. 2010; Ledésert et al. 2010; Vogt et al. 2012a, b; Vidal et al. 2017). Few studies, especially laboratory studies that offer values of porosity and permeability, have targeted the overlying Permo-Triassic sedimentary units (e.g. Haffen et al. 2013; Stober and Bucher 2015; Vidal et al. 2015; Griffiths et al. 2016). For example, Haffen et al. (2013) estimated the permeability of the Buntsandstein sandstones of EPS-1 using a portable TinyPerm II permeameter and found that their permeability ranges from 10^{-15} to 10^{-13} m². However, the laboratory measurements of Griffiths et al. (2016) highlight that the permeability of Buntsandstein sandstones from EPS-1 can be lower than 10^{-18} m².

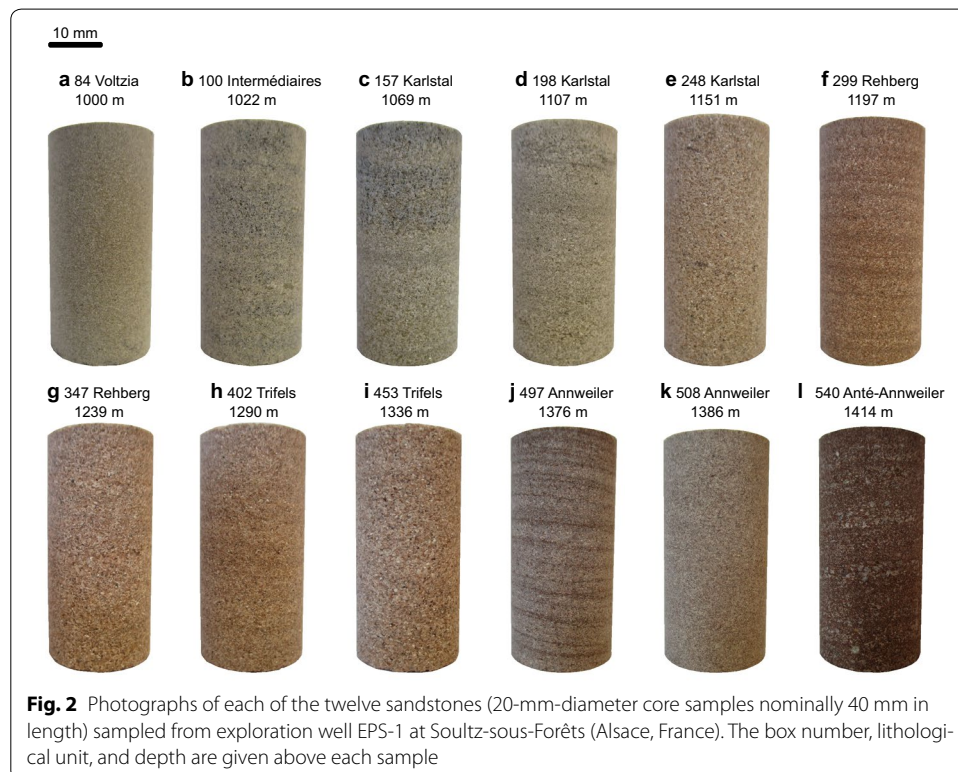
We present here a systematic microstructural (grain size and shape, specific surface area, pore size, and pore throat size distribution), mineralogical, and petrophysical (porosity, *P*-wave velocity, permeability) characterisation of the Buntsandstein sandstones, sampled from exploration well EPS-1 at the Soultz-sous-Forêts geothermal site (Fig. 1). EPS-1 was drilled vertically to a depth of 2227 m between 1990 and 1991 and continuous core was retrieved between the measured depths of 930 and 2227 m (all depths reported in this study are measured depths). The cored interval sampled the Triassic Muschelkalk unit (930–1000 m depth) and the Permo-Triassic Buntsandstein unit (1000–1417 m; Fig. 1b) directly overlying the granite basement (encountered at a depth of 1417 m). The Buntsandstein unit—the focus of this study—extends over large parts of west and central Europe (McCann 2008), and the formations specific to those found at Soultz-sous-Forêts can be readily identified in the wells drilled at Rittershoffen (Aichholzer et al. 2016), located ~ 6.5 km from the Soultz-sous-Forêts site (Fig. 1c). Therefore, although our study uses core material from Soultz-sous-Forêts, the data presented herein are likely relevant for current and future geothermal projects within the Upper



Rhine Graben. The continued development of geothermal energy is important to mitigate anthropogenic carbon emissions and therefore climate change (e.g. Fuss et al. 2014; Smith et al. 2016).

Material characterisation

The materials used for this study were taken from exploration well EPS-1 from the Soultz-sous-Forêts geothermal site (Fig. 1). The Buntsandstein was continuously cored at EPS-1 (1000–1417 m), to a core diameter of 78 mm. We sampled this continuous core material at regular (~ 40 to 50 m) depth intervals (between 1008 and 1414 m; Fig. 1b). Twelve samples (i.e. depths) were selected: one sandstone from the *Voltzia* unit, one from the *Couches Intermédiaires* unit, three from the *Karlstal* unit, two from the *Rehberg* unit, two from the *Trifels* unit, two from the *Annweiler* unit, and one from the *Anté-Annweiler* unit (Fig. 1b; see Aichholzer et al. (2016) for a complete stratigraphic column of the Permo-Triassic sedimentary units from the Soultz-sous-Forêts site). Seven or eight cylindrical samples (20 mm in diameter) were cored from each of the twelve borehole sandstones collected and precision-ground to a nominal length of 40 mm. These samples were cored so that their axes were parallel to the EPS-1 borehole (i.e. perpendicular to bedding). In addition, two cylindrical samples (of the same dimensions) of each of the twelve sandstones were prepared perpendicular to the borehole (i.e. parallel to bedding). A photograph of a 20-mm-diameter sample (prepared perpendicular to bedding) of each of the sampled intervals is given in Fig. 2. We complement these borehole samples with sandstones (all from the Buntsandstein) acquired from local quarries (Fig. 1c): one from Rothbach (from the *Karlstal* unit), one from Adamswiller (from the *Voltzia* unit), and one from Bust (from the *Voltzia* unit). Rocks from these quarries are used in the construction of buildings and monuments in Strasbourg and the surrounding area, including the iconic Notre Dame cathedral of Strasbourg. We prepared five samples of each of the three quarry rocks. The quarry rocks were cored perpendicular to bedding. All of the



samples were then washed and dried in a vacuum oven at 40 °C for at least 48 h. A total of 133 samples were prepared: 118 samples from the EPS-1 cores (94 perpendicular to bedding and 24 parallel to bedding) and 15 samples from the quarry rocks. For simplicity, the borehole samples in this study will be referred to by their box number (i.e. 84, 100, 157, 198, 248, 299, 347, 402, 453, 497, 508, and 540; see Table 1). Before measuring the permeability of the 133 samples—the main focus of this contribution—we first characterised the sandstones collected in terms of their porosity (connected and total), mineral content, specific surface area, microstructure, grain size and shape, and pore size and pore throat size distribution (pore throat size distribution was only determined for five of the borehole samples, see below).

Porosity

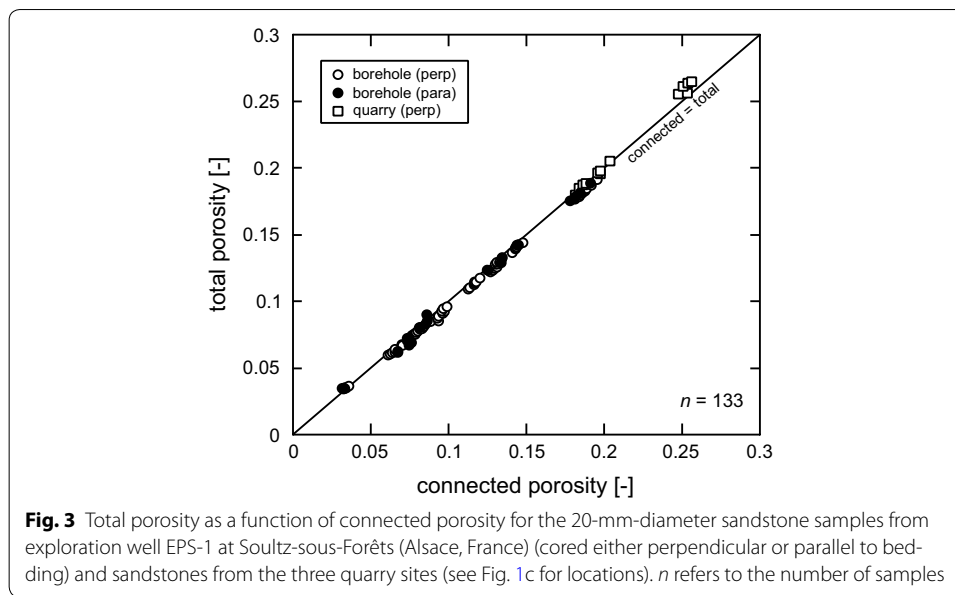
The connected porosity of each 20-mm-diameter sample was determined using a helium pycnometer (Micromeritics AccuPyc II 1340). The total porosity of each sample was calculated using their bulk density and the solid density of the material. The solid densities were determined by measuring the mass and volume (using the pycnometer) of powdered offcuts of each sample (powdered using a pestle-and-mortar). The average connected porosity of each of the sampled intervals is given in Table 1. A plot of the total porosity of these samples as a function of their connected porosity is shown in Fig. 3. The data of Fig. 3 show that the porosity of the EPS-1 samples ranges from ~ 0.03 to ~ 0.2, and that the porosity of the quarry samples ranges from ~ 0.18 to ~ 0.25. Figure 3 also shows that there is essentially no isolated porosity in the rocks studied, with the exception of the quarry rock from Adamswiller (the samples containing the highest porosity), which contains an isolated porosity of ~ 0.01.

Mineral content (X-ray powder diffraction)

Mineral content of the materials used in this study was quantified using X-ray powder diffraction (XRPD). Powdered sandstone samples were ground for 8 min with 10 ml of isopropyl alcohol in a McCrone Micronising Mill using agate cylinder elements. The XRPD analyses were performed on powder mounts using a PW 1800 X-ray diffractometer (CuK α , graphite monochromator, 10 mm automatic divergence slit, step-scan 0.02° 2 θ increments per second, counting time one second per increment, 40 mA, 40 kV). The phases in the whole rock powders were quantified using the Rietveld program BGMN (Bergmann et al. 1998). To identify the clay minerals, we also separated < 2 μ m fractions by gravitational settling and prepared oriented mounts that were X-rayed in an air-dried and an ethylene-glycolated state. The glycolated X-ray patterns were modelled using a structural model for R3 ordered illite–smectite (Ufer et al. 2012a, b). The illitic material in all samples is an R3-ordered illite–smectite with less than 10% smectite layers (about 5–6% smectite on average). The mineral content of each of the sandstones from the sampled intervals is given in Table 2. To better facilitate comparison, the mineral contents of the studied sandstones (borehole and quarry samples) are shown in pie charts in Fig. 4. In particular, we highlight that the lower *Annweiler* and *Anté-Annweiler* units and the upper *Voltzia* and *Couches Intermédiaires* units contain the highest proportions of clay, in accordance with previous investigations of the Buntsandstein from EPS-1 (e.g. Vernoux et al. 1995; Aichholzer et al. 2016). The illite–smectite in the Buntsandstein units is

Table 1 Average connected porosity, average grain diameter, average grain aspect ratio, average grain circularity, average grain roundness, and specific surface area for each of the twelve sandstones sampled from exploration well EPS-1 at the Soultz-sous-Forêts geothermal site (Alsace, France)

Box number	84	100	157	198	248	299	347	402	453	497	508	540
Depth (m)	1008	1022	1069	1107	1151	1197	1239	1290	1336	1376	1386	1414
Stratigraphic unit	Voltzia	Intermédiaires	Karlstal	Karlstal	Karlstal	Rehberg	Rehberg	Trifels	Trifels	Annweiler	Annweiler	Anté-Annweiler
Average connected porosity	0.096	0.065	0.117	0.097	0.144	0.130	0.185	0.131	0.189	0.034	0.082	0.075
Average grain diameter (µm)	142	306	424	192	294	332	367	259	361	291	199	379
Average grain aspect ratio	1.54	1.61	1.71	1.71	1.69	1.68	1.65	1.67	1.65	1.71	1.59	1.76
Average grain circularity	0.79	0.75	0.71	0.73	0.72	0.74	0.71	0.71	0.71	0.71	0.77	0.69
Average grain roundness	0.67	0.65	0.62	0.63	0.63	0.64	0.64	0.64	0.65	0.73	0.66	0.61
Specific surface area (m ² /kg)	1442	665	204	1485	1175	1888	1098	1349	1174	2024	2777	6170



considered to be the result of deep burial, tectonic events, and hydrothermal alteration (Vernoux et al. 1995). The large proportion of clay in the *Annweiler*, *Anté-Annweiler*, *Voltzia*, and *Couches Intermédiaires* units is thought to be a consequence of the high clay content of these sediments prior to burial and diagenesis (Vernoux et al. 1995).

Thermo-gravimetric analysis

To reinforce our mineralogical data (Table 2), we performed thermo-gravimetric analysis (TGA) on powdered samples (~ 55 to 60 mg) of each sandstone using a Netzsch Pegasus 404 thermal analysis device. Powders were heated in an atmosphere flushed with argon at a flow rate of 20 ml min^{-1} inside a platinum crucible (with lid). The powders were first heated to $100 \text{ }^\circ\text{C}$. This temperature was kept constant for 20 min to ensure that any free water (i.e. non-structurally bound) was removed. The powders were then subject to two heating–cooling cycles in which they were heated at $25 \text{ }^\circ\text{C min}^{-1}$ to $1050 \text{ }^\circ\text{C}$ and cooled back to room temperature at the same rate. This type of analysis tracks the mass loss of a sample as a result of, for example, the dehydroxylation of clays and the decarbonation of carbonates during heating. The mass loss data from these experiments (Fig. 5) are in agreement with our XRPD data (Table 2). Samples containing a high wt% of illite–smectite and/or dolomite suffer the greatest loss in mass (Fig. 5). The temperatures corresponding to the measured mass losses are in accordance with the dehydroxylation of illite–smectite (Earnest 1991a, b) and the decarbonation of dolomite (McIntosh et al. 1990). No mass changes were measured during the cooling cycle and the subsequent heating/cooling cycle, attesting to the completion of the devolatilization reactions.

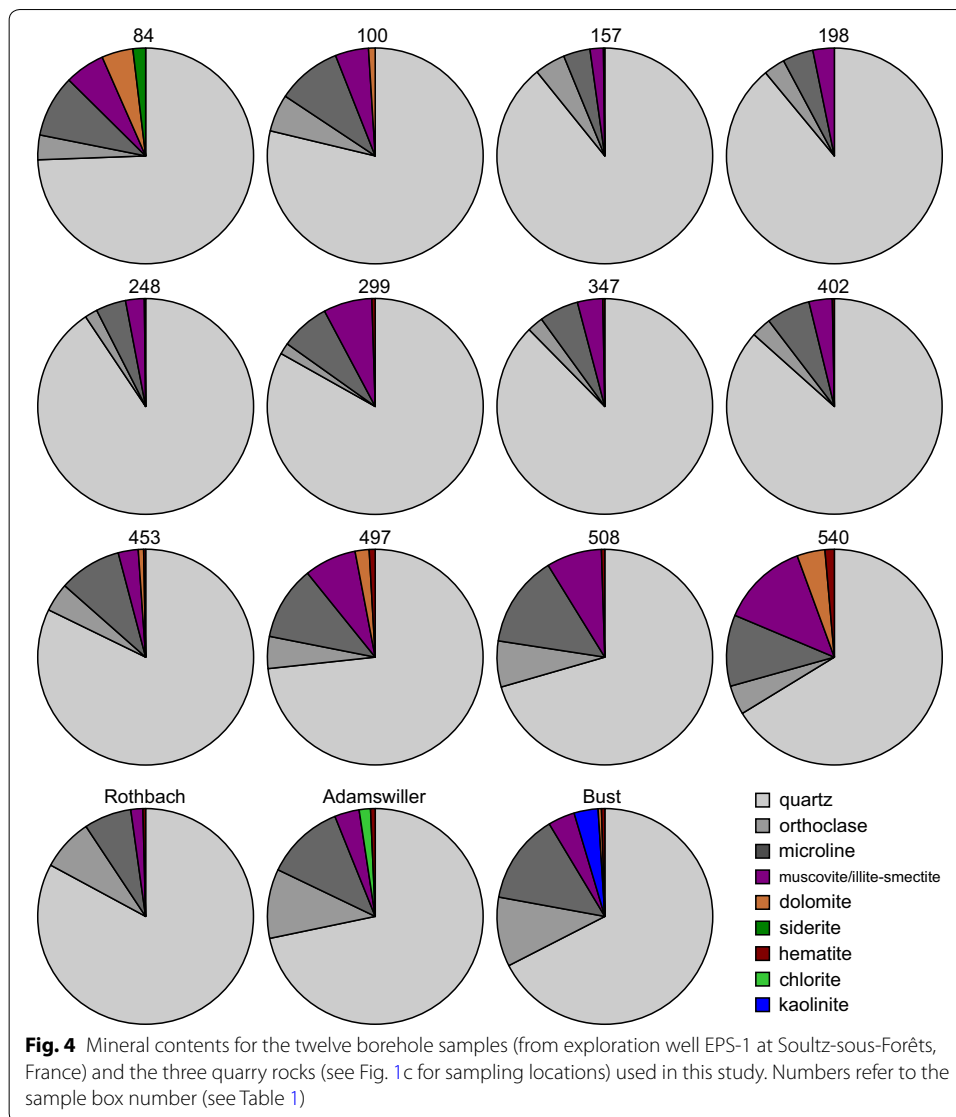
Specific surface area

The specific surface areas were measured using the Brunauer–Emmet–Teller (BET) nitrogen adsorption technique (by measuring the amount of adsorbate gas needed to create a monomolecular layer on the connected internal surface of the sample). The

Table 2 X-ray powder diffraction (XRPD) analysis showing quantitative bulk mineralogical composition for the twelve sandstones sampled from exploration well EPS-1 at the Soultz-sous-Forêts geothermal site (Alsace, France)

Box number	84	100	157	198	248	299	347	402	453	497	508	540
Depth (m)	1008	1022	1069	1107	1151	1197	1239	1290	1336	1376	1386	1414
Stratigraphic unit	Voltzia	Intermédiaires	Karlstal	Karlstal	Karlstal	Rehberg	Rehberg	Trifels	Trifels	Annweiler	Annweiler	Anté-Annweiler
Quartz	74.5 ± 1.6	78.9 ± 1.7	89.2 ± 0.4	89.0 ± 1.1	90.7 ± 1.2	83.4 ± 2.6	87.8 ± 1.3	86.7 ± 1.6	82.3 ± 1.7	73.3 ± 3.0	70.6 ± 2.8	66.4 ± 4.0
Orthoclase	3.7 ± 1.9	5.6 ± 0.0	4.6 ± 1.1	3.2 ± 0.2	1.9 ± 0.1	1.7 ± 0.2	2.4 ± 0.0	3.0 ± 0.8	4.3 ± 0.6	4.8 ± 0.4	6.9 ± 1.1	4.4 ± 0.9
Microcline	9.3 ± 0.8	9.7 ± 0.5	4.0 ± 1.7	4.6 ± 0.0	4.5 ± 0.2	7.4 ± 0.5	5.9 ± 0.1	6.6 ± 0.3	9.4 ± 0.4	11.1 ± 0.6	13.8 ± 0.5	10.7 ± 0.7
Muscovite/illite-Smectite	6.0 ± 2.9	5.0 ± 2.5	2.0 ± 0.8	3.2 ± 1.3	2.8 ± 1.3	7.3 ± 3.2	3.8 ± 1.5	3.5 ± 2.1	3.0 ± 1.8	7.8 ± 3.9	8.3 ± 4.5	13.1 ± 6.0
Dolomite	4.7 ± 0.1	1.0 ± 0.3	0.2 ± 0.1	-	-	-	-	-	0.8 ± 0.0	2.1 ± 0.0	-	4.2 ± 0.5
Siderite	1.9 ± 0.2	-	-	-	-	-	-	-	-	-	-	-
Haematite	-	-	-	-	0.2 ± 0.1	0.5 ± 0.1	0.3 ± 0.0	0.3 ± 0.0	0.3 ± 0.1	0.9 ± 0.1	0.5 ± 0.1	1.4 ± 0.1

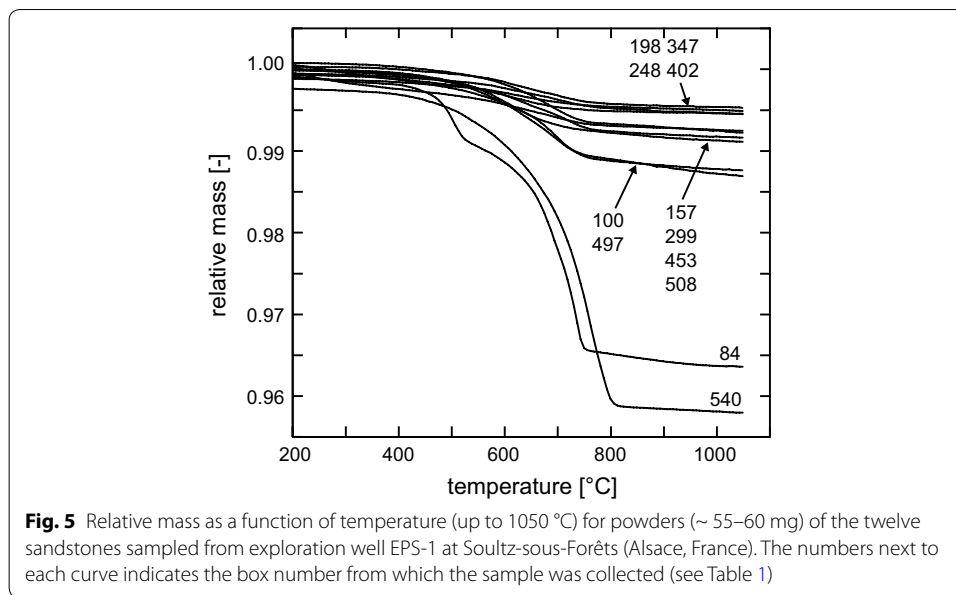
Values in wt%



specific surface area of each of the sandstones sampled from EPS-1, which varies from 204 to 6170 m²/kg, is given in Table 1.

Grain size and shape analysis

We determined grain size and shape descriptors for the sandstones sampled from EPS-1 using images of double-polished thin sections taken using a scanning electron microscope (SEM) (Tescan Vega 2 XMU). We first manually traced around all of the quartz grains in a ~ 20 mm² area on a backscattered SEM image (BSE) of each sample. These binary images were then analysed using open source software ImageJ. The number of grains analysed ranged from 200 to 700. The equivalent grain diameter, d , was calculated using $d = 3/2(d_F)$, where d_F is the average Feret diameter. Grain aspect ratio was defined as l_{major}/l_{minor} , where l_{major} and l_{minor} are the lengths of the major and minor axes of the best-fit ellipse, respectively. Grain “circularity” was defined as $4\pi \times g_a/g_p^2$, where g_a and g_p are the area and perimeter of a grain, respectively (where unity



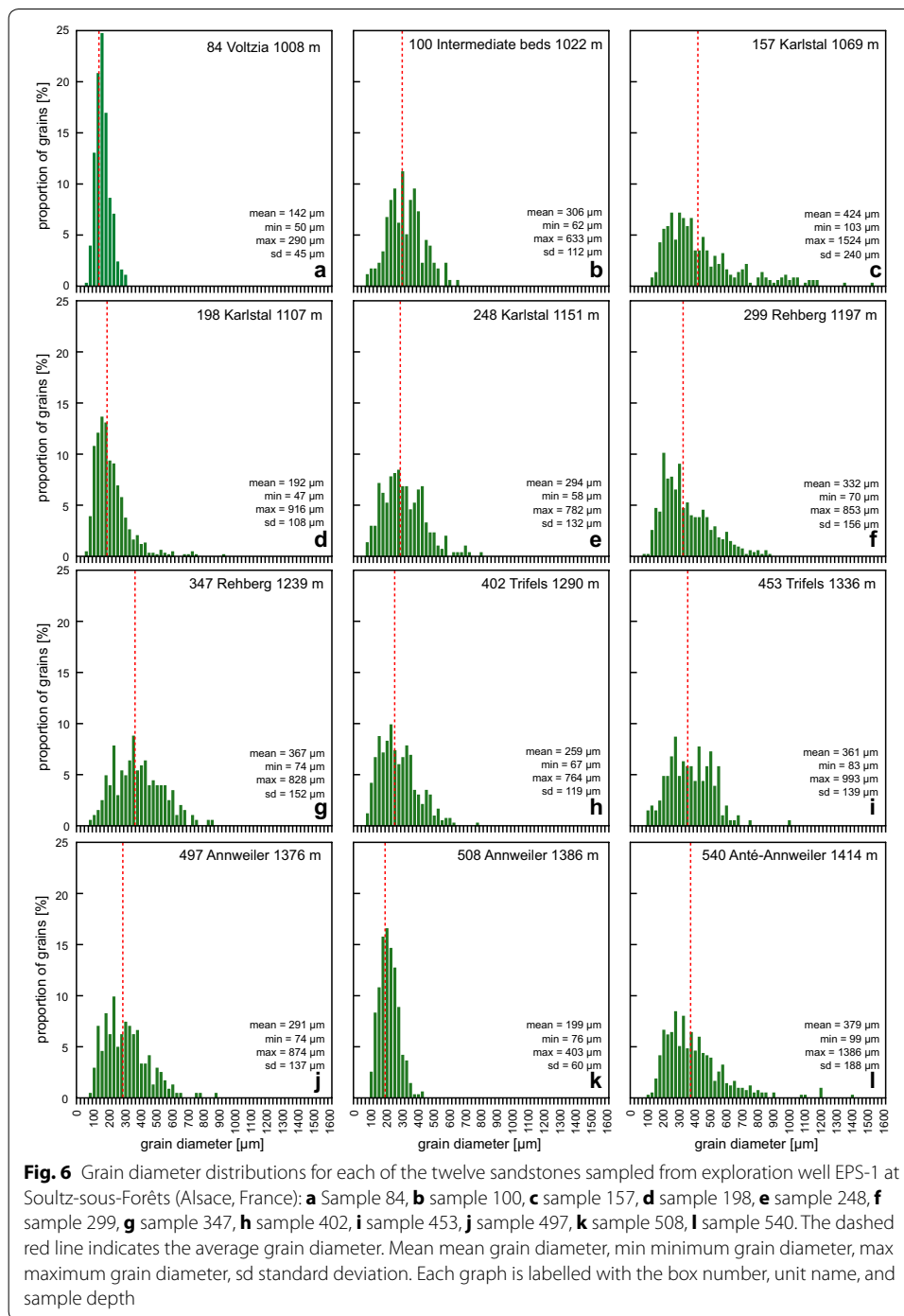
represents a perfect circle). Grain “roundness” was defined as $4 \times g_a / \pi \times (l_{major})^2$. The average grain diameter, \bar{d} , average grain aspect ratio, average grain circularity, and average grain roundness of each of the sandstones from the sampled intervals are given in Table 1. We find that the average grain diameter varies from 142 to 424 μm (Table 1). Average grain aspect ratio, average grain circularity, and average grain roundness are in the range 1.54–1.76, 0.69–0.79, and 0.61–0.73, respectively (Table 1). Figure 6 shows the grain size distribution for each of the sampled intervals (discussed in detail below). We highlight that these grain size and shape descriptors were determined from two-dimensional images and therefore only serve as an approximation of their true values.

Mercury porosimetry

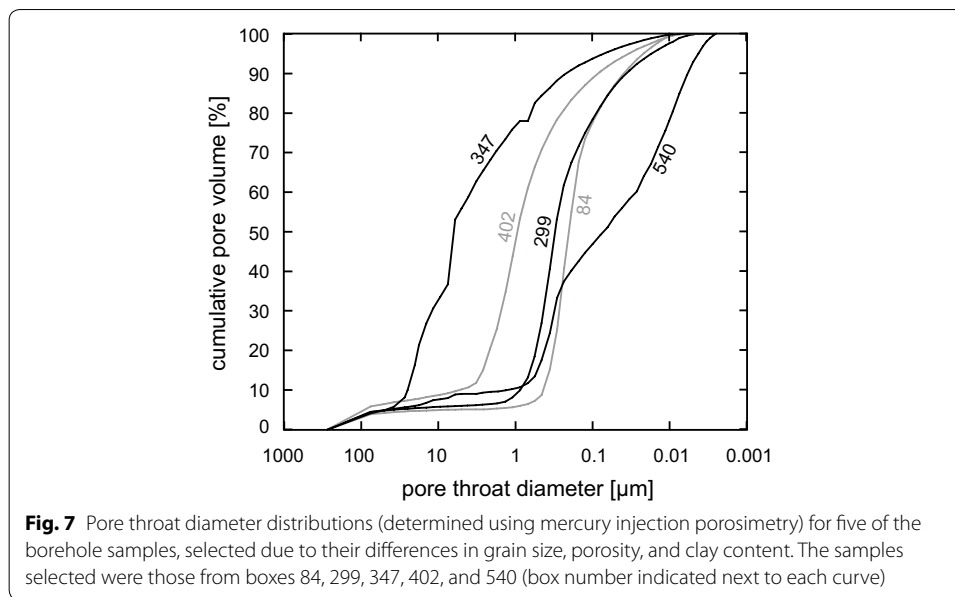
Mercury injection porosimetry was performed on five of the borehole samples: 84, 299, 347, 402, and 540. These samples were selected based on their differences in grain size, clay content, and porosity. Mercury injection data permit the calculation of the pore throat size distribution within a particular sample. We performed tests on pieces (2–7 g) of the aforementioned sandstones using the Micromeritics AutoPore IV 9500 at the University of Aberdeen. The evacuation pressure and evacuation time were 50 μmHg and 5 min, respectively, and the mercury filling pressure and equilibration time were 0.52 lb per square inch absolute (psia) and 10 s, respectively. The pressure range was 0.1 to 60,000 psia (i.e. up to a pressure of about 400 MPa). Figure 7 shows the pore throat diameter distribution for each of the five sandstones tested (discussed in detail below).

Descriptions of the twelve boreholes samples from EPS-1

The first sandstone (from box number 84), collected from a depth of 1008 m, is part of the *Voltzia* unit (Figs. 2a, 8a). It contains no obvious bedding/laminations (Figs. 2a, 8a). The sandstone has an average connected porosity of 0.096, an average grain diameter of 142 μm (fine sand), and a specific surface of 1442 m^2/kg (Table 1). The sandstone is



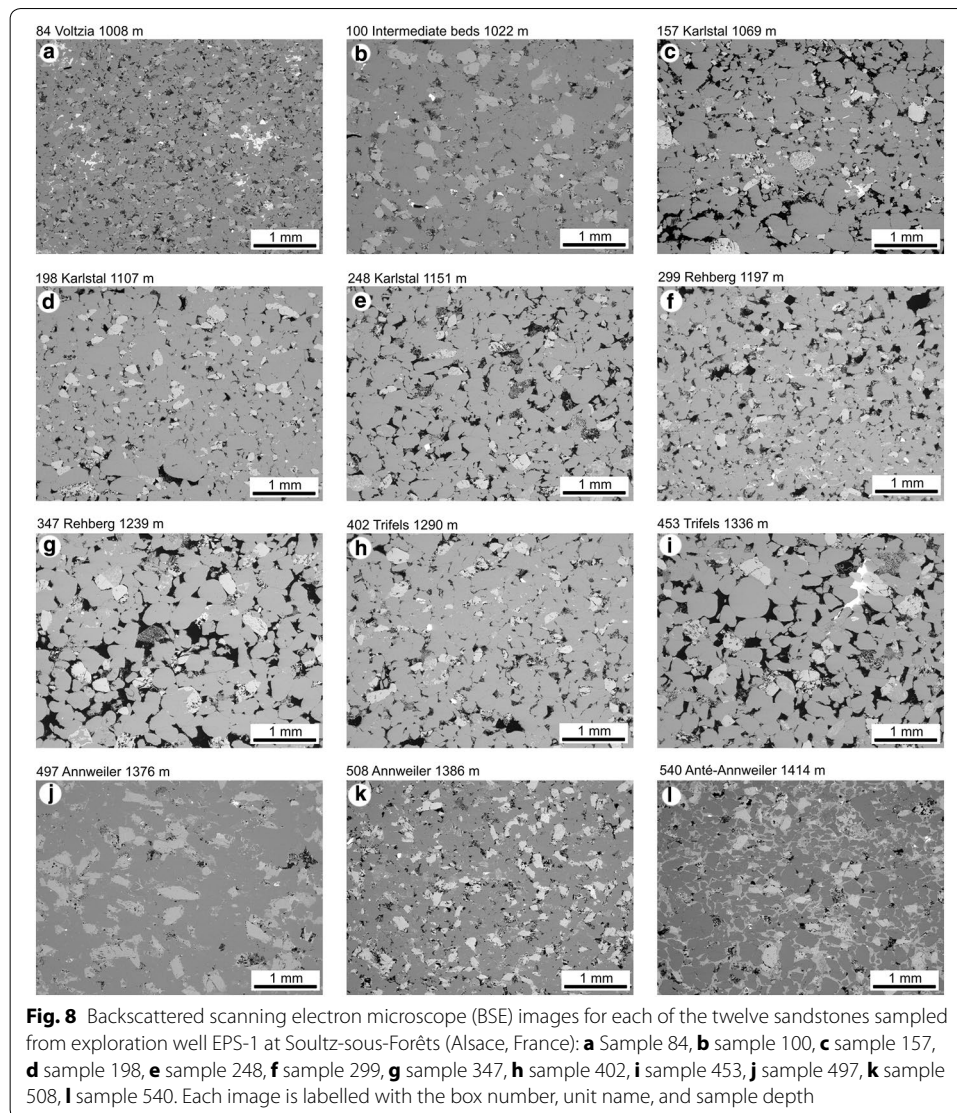
microstructurally homogenous and has a very narrow grain size distribution, exemplified by a low standard deviation of 45 μm (Fig. 6a). Sample 84 also has the lowest average aspect ratio, the highest grain circularity, and the second highest average grain roundness of the twelve depths sampled (Table 1). Pore diameters are typically less than 50 μm (Fig. 8a). The mercury injection data show that 95% of the pore volume is connected by pore throats with a diameter less than 1 μm (Fig. 7). Sample 84 is a feldspathic sandstone that contains ~ 75 wt% quartz, ~ 13 wt% feldspar (orthoclase and microcline), ~ 6



wt% muscovite/illite–smectite, ~ 5 wt% dolomite, and ~ 2 wt% siderite (Fig. 4; Table 2). The siderite (Fig. 9a), illite–smectite (Fig. 9b), and dolomite (Fig. 9b) occur as pore-filling minerals. This sandstone is thought to have been deposited in a fluvio-deltaic environment (Aichholzer et al. 2016).

The second sandstone (from box number 100), collected from a depth of 1022 m, is part of the *Couches Intermédiaires* unit (Figs. 2b, 8b). It contains no obvious bedding/laminations (Figs. 2b, 8b). This sandstone has an average connected porosity of 0.065, an average grain diameter of 306 μm (medium sand) (Fig. 6b), and a specific surface of 665 m^2/kg (Table 1). Pore diameters can reach ~ 100 μm , but are typically less than 50 μm (Fig. 8b). Sample 100 is a feldspathic sandstone that contains ~ 79 wt% quartz, ~ 15 wt% feldspar (orthoclase and microcline), ~ 5 wt% muscovite/illite–smectite, and ~ 1 wt% dolomite (Fig. 4; Table 2). The illite–smectite is found within the pores (Fig. 9c). We also found minor quantities of pore-filling barite (Fig. 9d), confirmed by energy-dispersive X-ray spectroscopy (EDS) during our SEM analysis (barite, although present, is below the detection level of our XRPD analysis). This sandstone is thought to reflect a braided fluvial system (Vernoux et al. 1995).

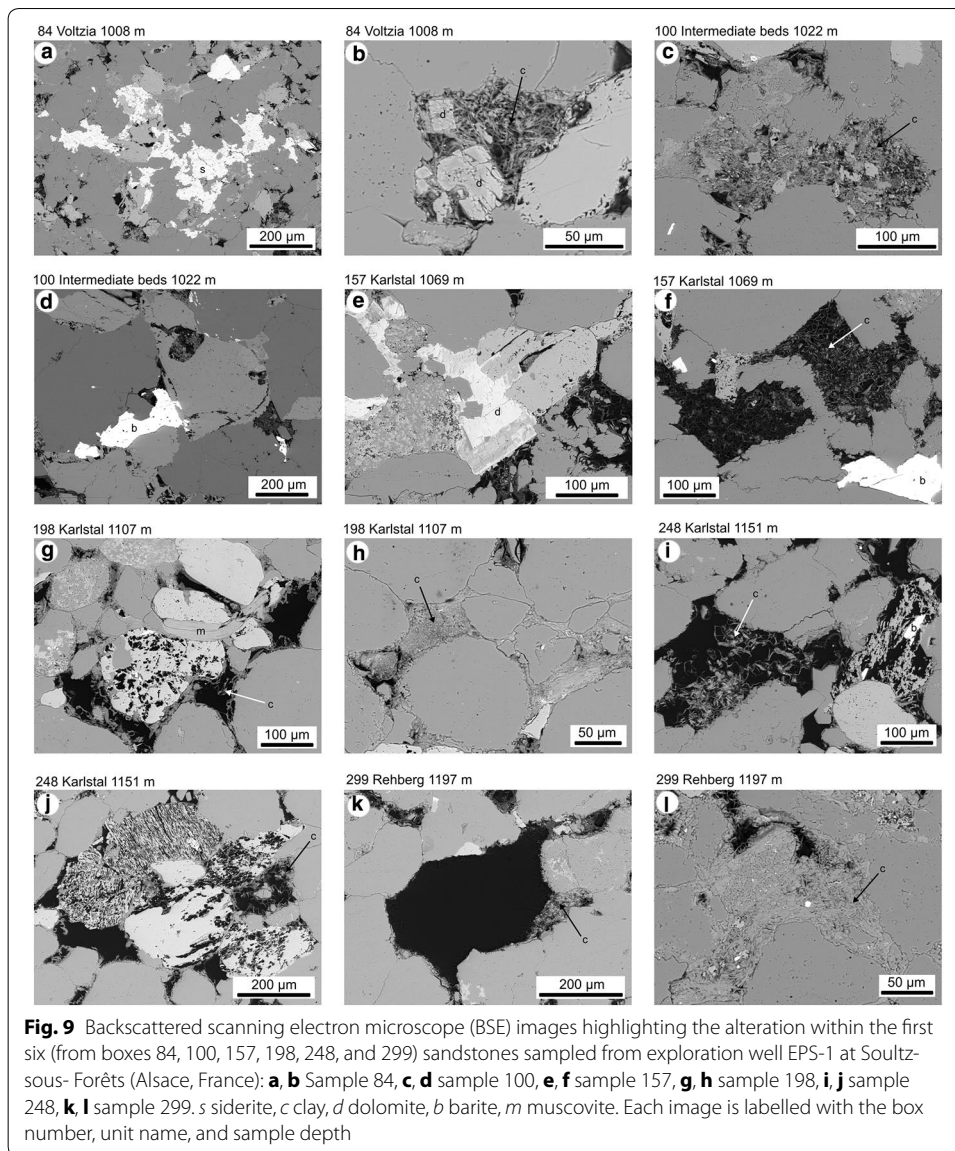
The third sandstone (from box number 157), collected from a depth of 1069 m, is part of the *Karlstal* unit (Figs. 2c, 8c). This aeolian (Aichholzer et al. 2016) sandstone has an average connected porosity of 0.117, an average grain diameter of 424 μm (medium sand), and a specific surface of 204 m^2/kg (Table 1). It contains alternating 1–2-mm-thick layers of high- and low-porosity bands, characterised by coarse (~ 800 μm) and fine-medium (~ 250 μm) grain sizes, respectively (Figs. 6c, 8c). As a result, the sandstone has a very wide grain size distribution (Fig. 6c). Pore diameters with the coarse layers are about 150 μm ; pores within the fine-medium layers are typically less than 50 μm (Fig. 8c). Sample 157 is a quartz-rich sandstone that contains ~ 89 wt% quartz, ~ 9 wt% feldspar (orthoclase and microcline), ~ 2 wt% muscovite/illite–smectite, and ~ 0.2 wt% dolomite (Fig. 4; Table 2). The dolomite (Fig. 9e) and illite–smectite (Fig. 9f) occur as



pore-filling minerals. We also found minor quantities of pore-filling barite (Fig. 9f), confirmed by EDS during our SEM analysis.

The fourth sandstone (from box number 198), collected from a depth of 1107 m, is part of the *Karlstal* unit (Figs. 2d, 8d). This aeolian (Aichholzer et al. 2016) sandstone has an average connected porosity of 0.097, an average grain diameter of 192 μm (fine sand), and a specific surface of 1485 m^2/kg (Table 1). It contains ~ 1 -mm-thick layers of low porosity that are characterised by a smaller grain size (below 100 μm) (Figs. 6d, 8d). Pore diameters are about 50 μm in the low-porosity layers, but can be up to a few hundred microns in the layers characterised by coarser grains and a higher porosity (Fig. 8d). Sample 198 is a quartz-rich sandstone that contains ~ 89 wt% quartz, ~ 8 wt% feldspar (orthoclase and microcline), and ~ 3 wt% muscovite/illite–smectite (Fig. 4; Table 2). The illite–smectite occurs as a pore-lining (Fig. 9g) or pore-filling (Fig. 9h) mineral. A number of the feldspar grains are altered (Fig. 9g).

The fifth sandstone (from box number 248), collected from a depth of 1151 m, is part of the *Karlstal* unit (Figs. 2e, 8e). It contains no obvious bedding/laminations (Figs. 2e,



8e). This aeolian (Aichholzer et al. 2016) sandstone has an average connected porosity of 0.144, an average grain diameter of 294 μm (medium sand) (Fig. 6e), and a specific surface of 1175 m^2/kg (Table 1). The pores in sample 248 are typically between 50 and 150 μm in diameter (Fig. 8e). Sample 248 is a quartz-rich sandstone that contains ~ 91 wt% quartz, ~ 6.5 wt% feldspar (orthoclase and microcline), ~ 3 wt% muscovite/illite-smectite, and ~ 0.2 wt% haematite (Fig. 4; Table 2). The illite-smectite occurs as a pore-lining or pore-filling mineral (Figs. 9i, j). We also found minor quantities of barite (Fig. 9i), confirmed by EDS during our SEM analysis, and altered feldspar grains (Fig. 9j).

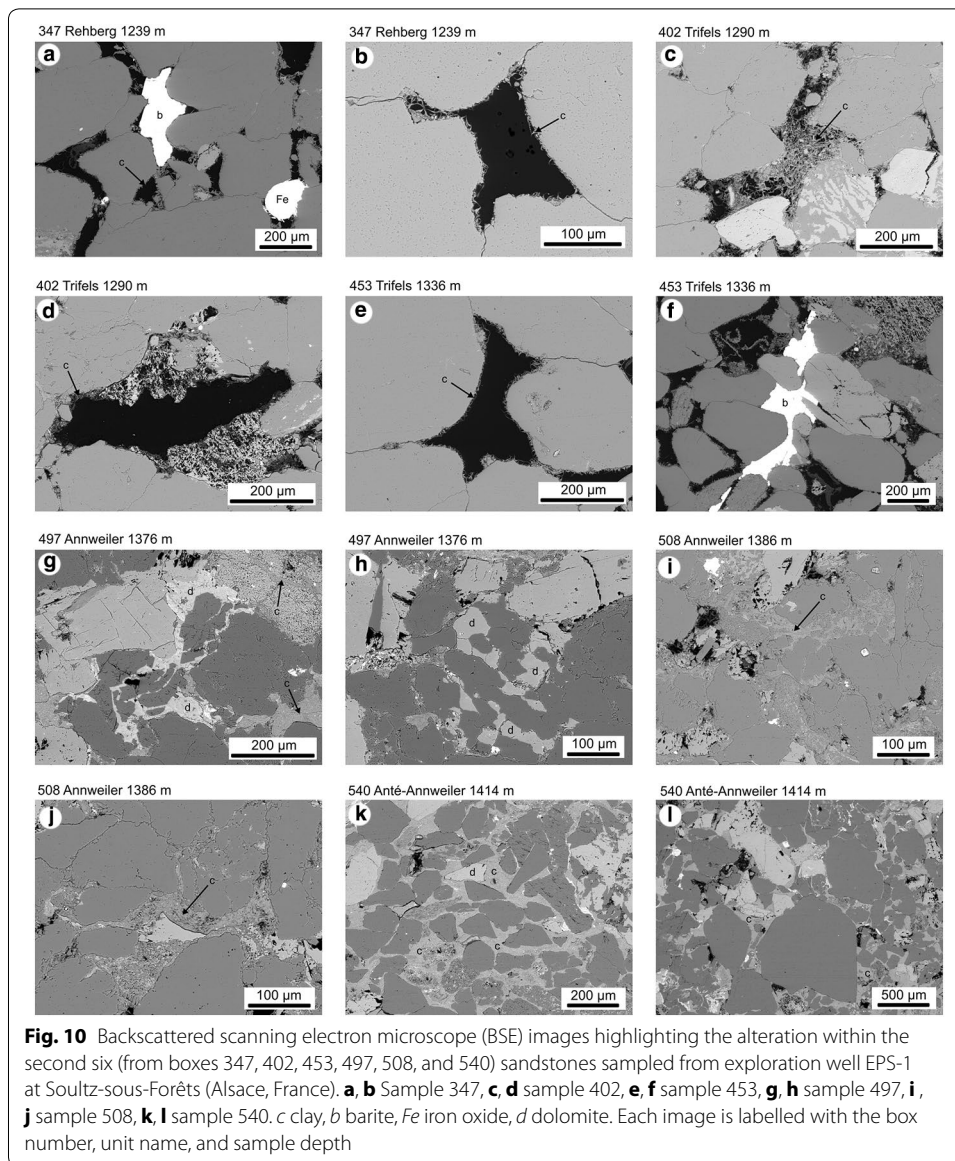
The sixth sandstone (from box number 299), collected from a depth of 1197 m, is part of the *Rehberg* unit (Figs. 2f, 8f). This sandstone has an average connected porosity of 0.130, an average grain diameter of 332 μm (medium sand), and a specific surface of 1888 m^2/kg (Table 1). It contains alternating layers (~ 1 mm thick) of high and low porosity (Fig. 6f), characterised by medium-coarse (~ 500 μm) and fine (~ 200 μm) grain sizes, respectively (Figs. 6f, 8f). As a result, the sandstone has a wide grain size distribution (Fig. 6f). The pores

within sample 299 also have a wide distribution: pores within the high-porosity layers can be a few hundred microns in diameter, but are much smaller (diameters of a few tens of microns) in the low-porosity layers (Fig. 8f). The mercury injection data show that 90% of the pore volume is connected by pore throats with a diameter less than 1 μm (Fig. 7). Sample 299 is a quartz-rich sandstone that contains ~ 83 wt% quartz, ~ 9 wt% feldspar (orthoclase and microcline), ~ 7 wt% muscovite/illite–smectite, and ~ 0.5 wt% haematite (Fig. 4; Table 2). The illite–smectite occurs as a pore-lining (Fig. 9k) or pore-filling (Fig. 9l) mineral. This sandstone is thought to have been deposited in a fluvial environment (Aichholzer et al. 2016).

The seventh sandstone (from box number 347), collected from a depth of 1239 m, is part of the *Rehberg* unit (Figs. 2g, 8g). It contains no obvious bedding/laminations (Figs. 2g, 8g). This fluvial (Aichholzer et al. 2016) sandstone has an average connected porosity of 0.185, an average grain diameter of 367 μm (medium sand) (Fig. 6g), and a specific surface of 1098 m^2/kg (Table 1). The pore diameter in sample 347 can be as large as ~ 250 μm (Fig. 8g). The mercury injection data show that pore throats with a diameter greater than 10 μm connect 35% of the pore volume, $\sim 45\%$ is connected by pore throats between 1 and 10 μm in diameter, and that only $\sim 20\%$ is connected by pore throats with a diameter less than 1 μm (Fig. 7). Sample 347 is a quartz-rich sandstone that contains ~ 88 wt% quartz, ~ 8 wt% feldspar (orthoclase and microcline), ~ 4 wt% muscovite/illite–smectite, and ~ 0.3 wt% haematite (Fig. 10a) (Fig. 4; Table 2). The illite–smectite typically occurs as a pore-lining mineral (Fig. 10a, b). We also found minor quantities of pore-filling barite (Fig. 10a), confirmed by EDS during our SEM analysis.

The eighth sandstone (from box number 402), collected from a depth of 1290 m, is part of the *Trifels* unit (Figs. 2h, 8h). This fluvial (Aichholzer et al. 2016) sandstone has an average connected porosity of 0.131, an average grain diameter of 259 μm (medium sand), and a specific surface of 1349 m^2/kg (Table 1). It contains alternating layers (~ 1 mm thick) of high and low porosity that are related to differences in cementation and compaction (Fig. 8h), rather than a major difference in grain size (Fig. 6h). Pore diameter can be as high as ~ 250 to 250 μm in the high-porosity layers, but is typically 50 μm , or less, in the layers of low porosity (Fig. 8g). The mercury injection data show that $\sim 60\%$ of the pore volume is connected by pore throats with a diameter greater than 1 μm (Fig. 7). Sample 402 is a quartz-rich sandstone that contains ~ 87 wt% quartz, ~ 10 wt% feldspar (orthoclase and microcline), ~ 3.5 wt% muscovite/illite–smectite, and ~ 0.3 wt% haematite (Fig. 4; Table 2). The illite–smectite occurs as a pore-filling (Fig. 10c) or pore-lining (Fig. 10d) mineral. A number of the feldspar grains were found altered (Fig. 10d).

The ninth sandstone (from box number 453), collected from a depth of 1336 m, is part of the *Trifels* unit (Figs. 2i, 8i). It contains no obvious bedding/laminations (Figs. 2i, 8i). This fluvial (Aichholzer et al. 2016) sandstone has an average connected porosity of 0.189, an average grain diameter of 361 μm (medium sand) (Fig. 6i), and a specific surface of 1174 m^2/kg (Table 1). The pores in sample 453 are typically 100–200 μm in diameter (Fig. 8i). Sample 453 is a feldspathic sandstone that contains ~ 82 wt% quartz, ~ 14 wt% feldspar (orthoclase and microcline), ~ 3 wt% muscovite/illite–smectite, ~ 1 wt% dolomite, and ~ 0.3 wt% haematite (Fig. 4; Table 2). The illite–smectite occurs as a pore-lining mineral (Fig. 10e). We also found minor quantities of pore-filling barite (Fig. 10f), confirmed by EDS during our SEM analysis.



The tenth sandstone (from box number 497), collected from a depth of 1376 m, is part of the *Annweiler* unit (Figs. 2j, 8j). Although this sandstone is Permian in age (all of the above-described units are Triassic), it is often considered as part of the Buntsandstein unit (the *Annweiler* unit and *Anté-Annweiler* unit, described below, are sometimes collectively referred to as the *Buntsandstein Inférieur*; Aichholzer et al. 2016). In this study, we will consider these Permian units (the *Annweiler* and *Anté-Annweiler* units) as part of the Buntsandstein. This sandstone has an average connected porosity of 0.034, an average grain diameter of 291 μm (medium sand), and a specific surface of 2024 m^2/kg (Table 1). It contains a distinct lamination, consisting of alternating light- and dark red/brown layers that are 1–2 mm in thickness. These laminations are not associated with notable changes to porosity (Fig. 8j) or grain size (Fig. 6j). Pores are often only a couple of microns in diameter, but can be as large as 50 or even 100 μm (Fig. 8j). Sample 497 is a feldspathic sandstone that contains ~ 73 wt% quartz, ~ 16 wt% feldspar (orthoclase

and microcline), ~ 8 wt% muscovite/illite–smectite, ~ 2 wt% dolomite, and ~ 1 wt% haematite (Fig. 4; Table 2). The illite–smectite and dolomite occur as pore-filling minerals (Fig. 10g, h), significantly reducing the porosity of the sandstone (Table 1). This sandstone is thought to be continental in origin (debris cone/fluvial environment) (Aichholzer et al. 2016).

The eleventh sandstone (from box number 508), collected from a depth of 1386 m, is part of the *Annweiler* unit (Figs. 2k, 8k). It contains no obvious bedding/laminations (Figs. 2k, 8k). This Permian sandstone has an average connected porosity of 0.082, an average grain diameter of 199 μm (fine sand), and a specific surface of 2777 m^2/kg (Table 1). The sandstone is macro- and microstructurally homogenous and has a very narrow grain size distribution, exemplified by a low standard deviation of 60 μm (Fig. 6k). Further, the grains forming sample 508 are characterised by a relatively low average aspect ratio and a relatively high average grain circularity and average grain roundness (Table 1). The pores in sample 508 are typically between 50 and 100 μm (Fig. 8k). Sample 508 is a feldspathic sandstone that contains ~ 71 wt% quartz, ~ 21 wt% feldspar (orthoclase and microcline), ~ 8 wt% muscovite/illite–smectite, and ~ 0.5 wt% haematite (Fig. 4; Table 2). The illite–smectite occurs as a pore-filling mineral (Fig. 10i, j). This sandstone is thought to be continental in origin (debris cone/fluvial environment) (Aichholzer et al. 2016).

The twelfth sandstone (from box number 540), collected from a depth of 1414 m, is part of the *Anté-Annweiler* unit (Figs. 2l, 8l). This sandstone is Permian in age and is part of the unit that directly overlies the granitic basement. It contains distinct layers (3–4 mm in thickness) characterised by the absence (Fig. 10k) or presence (Fig. 10l) of coarse to very coarse (1–2 mm in diameter) angular grains. As a result, the sandstone has a very wide grain size distribution (Fig. 6l). The grains forming sample 540 have the highest average aspect ratio and the lowest average grain circularity and average grain roundness of the twelve depths sampled (Table 1). This sandstone has an average connected porosity of 0.075, an average grain diameter of 379 μm (medium sand), and a specific surface of 6170 m^2/kg (Table 1). The pores in sample 540 are typically between 50 and 100 μm (Fig. 8l). The mercury injection data show that two families of pore throat size exist (Fig. 7). The data show that ~ 25% of the pore volume is connected by pore throats with a diameter between 0.4 and 1 μm , and that pore throats with a diameter between 0.04 and 0.004 μm connect ~ 40% of the pore volume (Fig. 7). Sample 540 is a feldspathic sandstone that contains ~ 66 wt% quartz, ~ 15 wt% feldspar (orthoclase and microcline), ~ 13 wt% muscovite/illite–smectite, ~ 4 wt% dolomite, and ~ 1.5 wt% haematite (Fig. 4; Table 2). This sandstone contains much more clay than the other sandstones collected. Indeed, the quartz, feldspar, and dolomite grains appear to “float” within an illite–smectite matrix (Figs. 8l, 10k, l). This sandstone is thought to be continental in origin (debris cone/fluvial environment) (Aichholzer et al. 2016).

Descriptions of the three quarry rocks

The three quarry rocks are from quarries near the towns of Rothbach (Carrière Loegel Rothbach), Adamswiller (Rauscher SA Adamswiller), and Bust (Scheider Georges et Fils Bust) (Fig. 1). Rothbach and Adamswiller sandstones have been extensively used in previous experimental studies (e.g. David et al. 1994; Wong et al. 1997; Zhu et al. 1997; Zhu and

Table 3 X-ray powder diffraction (XRPD) analysis showing quantitative bulk mineralogical composition for the three quarry rocks (see Fig. 1c for quarry locations)

Rock name	Rothbach	Adamswiller	Bust
Depth (m)	quarry	quarry	quarry
Stratigraphic unit	Karlstal	Voltzia	Voltzia
Quartz	82.8 ± 0.5	71.8 ± 0.6	67.4 ± 1.0
Orthoclase	7.8 ± 0.2	10.4 ± 0.2	10.4 ± 0.2
Microcline	7.1 ± 0.2	11.8 ± 0.5	13.5 ± 0.5
Muscovite/Illite–Smectite	1.8 ± 0.5	3.7 ± 1.0	4.0 ± 1.0
Kaolinite	–	–	3.6 ± 0.5
Chlorite	–	1.7 ± 0.2	–
Dolomite	–	–	0.5 ± 0.1
Siderite	–	–	–
Haematite	0.4 ± 0.2	0.7 ± 0.2	0.5 ± 0.1

Values in wt%

Wong 1997; Bésuelle et al. 2003; Baud et al. 2004; Louis et al. 2005; Baud et al. 2006; Tembe et al. 2007; Louis et al. 2009). Rothbach sandstone is from the *Karlstal* unit, and Adamswiller and Bust sandstones are from the *Voltzia* unit. They have an average connected porosity of 0.191, 0.253, and 0.192, respectively. All three quarry rocks are feldspathic sandstones (Table 3) with a relatively low clay content compared to the rocks from the borehole (Fig. 4; Table 2). Unseen in the borehole samples, Adamswiller sandstone contains 1.7 wt% of chlorite and Bust sandstone contains 3.6 wt% of kaolinite (Fig. 4; Table 3).

Rothbach sandstone contains alternating layers that show differences in porosity and grain size (Louis et al. 2005, 2009). The more porous layers contain larger grains (with diameters in the range 200–250 μm, i.e. fine-medium sand) than the lower porosity layers (with diameters in the range 100–150 μm, i.e. very fine–fine sand) (Louis et al. 2005, 2009). Adamswiller sandstone has an average grain diameter of 120 μm (very fine sand) (David et al. 1994). Adamswiller and Bust sandstones contain no obvious bedding/laminations, although Adamswiller is known to exhibit a mechanical anisotropy (Baud et al. 2005).

Laboratory methods: measuring permeability and P-wave velocity

Measuring permeability in the laboratory

Permeability—the main focus of this contribution—was measured on oven-dry (hereafter simply called “dry”) samples using a benchtop gas (nitrogen) permeameter (schematic provided in Farquharson et al. 2016; Heap and Kennedy 2016) either in a steady-state setup (for high permeabilities) or in a pulse decay setup (for low permeabilities). All permeability measurements were conducted under a confining pressure, P_c , of 1 MPa.

For the steady-state method, volumetric flow rate, Q_v , measurements were taken (using a gas flowmeter) for several pressure gradients, ΔP (defined here as the upstream pore fluid pressure, P_u , minus the downstream pore fluid pressure, P_d). In our setup, P_d is simply the atmospheric pressure (taken here to be 101,325 Pa). Values of ΔP were typically from 0.005 to 0.2 MPa, equating to flow rates between 10 and 500 ml min⁻¹. Darcian permeability, k_D , was then calculated for each ΔP using the following relation:

$$k_D = \frac{Q_v}{P_m \Delta P} \frac{\mu L P_d}{A}, \quad (1)$$

where P_m is the mean pore fluid pressure (i.e. $(P_u + P_d)/2$); μ is the viscosity of the pore fluid (taken as the viscosity of nitrogen at 20 °C = 1.76×10^{-5} Pa s); and L and A are the sample length and cross-sectional area, respectively.

The reason for measuring k_D for different values of ΔP is to assess the Darcian permeability (Eq. 1) for fluid flow-related artefacts: turbulent flow (i.e. the Forchheimer effect; Forchheimer 1901) and/or gas slip along flow channel walls (i.e. the Klinkenberg effect; Klinkenberg 1941). We first plot $1/k_D$ for each ΔP as a function of Q_v to check whether the Forchheimer correction is required. The Forchheimer correction is necessary if the data are well described by a positive linear relationship. The Forchheimer-corrected permeability k_{forch} is taken as the inverse of the y -intercept of the best-fit linear regression of this positive linear relationship. If the Forchheimer correction is required, we then check whether the Klinkenberg correction is required. To do this, k_{forch} is calculated for each ΔP using:

$$\frac{1}{k_D} = \xi Q_v + \frac{1}{k_{\text{forch}}}, \quad (2)$$

where ξ , not strictly needed in this analysis, is the slope of the plot of $1/k_D$ as a function of Q_v . k_{forch} is then assessed as a function of $1/P_m$. The Klinkenberg correction is necessary if these data are well described by a positive linear relationship, and the true permeability is taken as the y -intercept of the best-fit linear regression of the data. If the data on the plot of k_{forch} as a function of $1/P_m$ cannot be described by a positive linear slope, then the true permeability is taken as k_{forch} (i.e. the inverse of the y -intercept of the best-fit linear regression on the graph of $1/k_D$ as a function of Q_v).

In the absence of a Forchheimer correction, the need for a Klinkenberg correction is determined by assessing k_D as a function of $1/P_m$. A Klinkenberg correction is deemed necessary if these data can be well described by a positive linear relationship. The true sample permeability is given by k_{klink} —the y -intercept of the best-fit linear regression on the plot of k_D as a function of $1/P_m$. k_D is taken as the true permeability if no corrections are required and is given by the slope of the graph of Q_v as a function of ΔP multiplied by the mean pore fluid pressure P_m .

When the permeability of a sample was too low to be measured using our flowmeters (i.e. $< 10^{-17}$ m²), we used the pulse decay method (Brace et al. 1968). k_D is determined using this method by monitoring the equilibration of pore fluid pressure across a permeable sample separated by two fixed-volume reservoirs (Brace et al. 1968). These measurements are conducted by increasing the pressure in the upstream pore fluid reservoir, P_u and monitoring the decay of P_u across the sample until $P_u = P_d = P_f$, where P_f is the final, equilibrated pore fluid pressure across the whole system. The decay of P_u is described by:

$$P_u - P_f = \Delta P \left(\frac{V_d}{V_u} + V_d \right) e^{-\alpha t}, \quad (3)$$

where t is time, and V_u and V_d are the volumes of the upstream and downstream reservoirs, respectively, and

$$\alpha = \frac{k_D A}{\mu \beta L} \left(\frac{1}{V_u} - \frac{1}{V_d} \right), \quad (4)$$

where β is the compressibility of the pore fluid, which is assumed to be constant at constant temperature (Brace et al. 1968). Using this method, $-\alpha$ is the slope of the plot of $\log(P_u - P_f)$ as a function of t and Eq. (4) is solved for k_D . The pulse decay method requires the application of a small pore pressure pulse to ensure that the effective pressure ($P_{\text{eff}} = P_c - P_m$) acting on the sample is approximately constant, thus avoiding pressure-induced changes to microstructure (e.g. microcrack closure).

In our system, the gas from the upstream pore fluid reservoir is allowed to evacuate to ambient laboratory conditions, thus V_d is infinite and P_d is equal to atmospheric pressure. To perform such measurements, we first maintain P_u is at a constant pressure of 0.2 MPa using a gas bottle for at least 1 h; this allows for complete pore fluid saturation of the sample. The upstream pore fluid reservoir is then isolated from the gas bottle using a valve and P_u is allowed to decay from this fixed volume, V_u , to ambient laboratory conditions.

We note that Eq. (3) requires that the compressibility of the pore fluid remains constant. However, if the downstream reservoir is infinite (i.e. the pore fluid is allowed to vent to the atmosphere), the pore fluid compressibility varies significantly as it approaches atmospheric pressure. To account for this variability in compressibility, we consider that the volumetric gas flux, $q_v = \frac{Q_v}{A}$, across any cross-sectional area, A , of the sample can be described by

$$\frac{Q_v}{A} = \frac{-k_D}{\mu} \frac{\partial P}{\partial x}, \tag{5}$$

where ∂x is some distance along the length of the sample. As in the steady-state method, we assume that the mass flux of gas across the sample cross section at any point, x , is constant for any given moment in time (i.e. the sample cannot store any fluid). Further, we assume that the temperature across the sample length is constant. Equation (5) can be recast in terms of mass flow rate, Q_M

$$\frac{Q_M}{\rho A} = \frac{Q_v}{A} = \frac{-k_D}{\mu} \frac{\partial P}{\partial x}. \tag{6}$$

Since both Q_M and P_u are functions of time, we define $Q_M = dm/dt$, where m is the mass of gas. By applying the ideal gas law, $PV = mRT/M$, where for a volume, V , of gas, P is the pressure of the gas, M is the molar mass of the gas, R is the ideal gas constant, and T is temperature, Q_M can be re-written and substituted into Eq. (6) to give (defining the gas density as $\rho = m/v = MP/(RT)$)

$$\frac{V}{PA} \frac{dP}{dt} = \frac{-k_D}{\mu} \frac{\partial P}{\partial x}. \tag{7}$$

Applying Eq. (7) to the interface between the upstream reservoir and the sample ($x = 0$), assuming that the upstream reservoir evacuates to an infinite downstream reservoir across the sample, and integrating along L yields

$$k_D = \frac{2L\mu}{A} \frac{V_u}{P_u^2 - P_d^2} \frac{dP_u}{dt}. \tag{8}$$

To calculate the permeability of a sample using Eq. (8), V_u must be accurately known. This volume can be determined experimentally by recording Q_v and the upstream pressure decay (dP_u/dt) contemporaneously. Assuming conservation of mass between the sample inlet ($x = 0$) and the sample outlet ($x = L$) and that the temperature in both reservoirs is equal, we arrive at

$$Q_M = \frac{M}{RT} P_u Q_{V_u} = \frac{M}{RT} P_d Q_{V_d}, \quad (9)$$

where Q_{V_u} and Q_{V_d} are the volumetric flow rates measured at the entrance and exit of the sample, respectively. Since $Q_M = \frac{M}{RT} \frac{dP_u}{dt} V_u$ and $\frac{\partial P_u}{\partial t} V_u = P_d Q_{V_d}$ we have

$$V_u = \frac{P_d Q_{V_d} \partial t}{\partial P_u}. \quad (10)$$

If the downstream reservoir is infinite, the upstream reservoir volume is given by the slope of Q_{V_d} as a function of dP_u/dt , multiplied by atmospheric pressure (since P_d is equal to the atmospheric pressure).

To assess the relevance of a Klinkenberg effect, k_D is calculated for every time step and is plotted as a function of $1/P_m$. If these data are well described by a positive linear relationship, then a Klinkenberg effect is observed and the true sample permeability is taken as the intercept of the linear regression that describes the data.

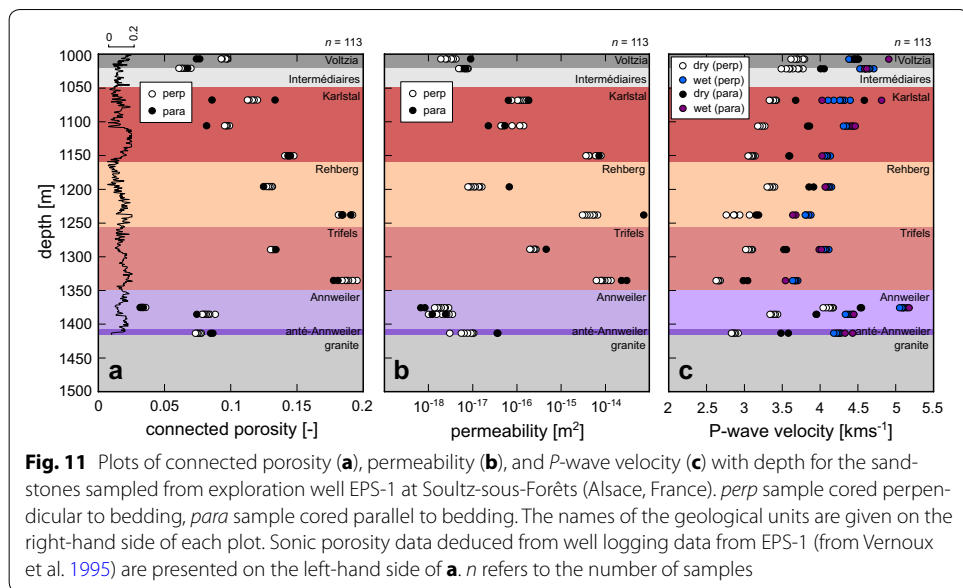
Measuring P -wave velocity in the laboratory

We characterised all the prepared samples in terms of their P -wave velocity. P -wave velocity was measured along the axis of each sample using piezoelectric sensors excited at a frequency of 700 kHz. The time of the first arrival of the signal through the sample was used to calculate the P -wave velocity. All measurements were conducted under a uniaxial stress of ~ 1 MPa. P -wave velocities were first measured on the dry samples, and again following vacuum saturation with deionised water (hereafter called “wet”).

Results

Connected porosity, permeability, and P -wave velocity (dry and wet) are plotted as a function of depth in Fig. 11 (we recall that porosity and P -wave velocity were measured under ambient laboratory pressure, and that permeability was measured under a confining pressure of 1 MPa). These data are also available in Table 4.

Our data show that connected porosity increases with depth up to the base of the *Trifels* unit, from 0.06 to 0.1 in the *Voltzia* unit up to almost 0.2 in the *Trifels* unit (Fig. 11a). In detail, porosity increases from ~ 0.06 at a depth of ~ 1000 m up to ~ 0.13 at ~ 1150 m (near the base of the *Karlstal* unit); porosity then increases up to ~ 0.2 at a depth of ~ 1340 m (near the base of the *Trifels* unit). The units directly below the *Trifels* unit—the *Annweiler* and *Anté-Annweiler* units—are characterised by much lower porosities, between 0.03 and 0.08 (Fig. 11a). Although our samples do not contain meso- or macroscale fractures, our porosity data are in general agreement with the sonic porosity data deduced from well logging data (Vernoux et al. 1995) (Fig. 11a). There are no significant or systematic differences between the porosity of samples cored parallel and perpendicular to bedding (Fig. 11a).



Permeability as a function of depth (Fig. 11b) follows a trend very similar to porosity with depth (Fig. 11a). Figure 11b shows that permeability increases from $\sim 10^{-18} \text{ m}^2$ in the *Voltzia* unit up to $\sim 10^{-15}$ to 10^{-14} m^2 in the *Trifels* unit (Fig. 11b), and that permeability is much lower in the deeper *Annweiler* and *Anté-Annweiler* units (Fig. 11b). The lowest permeabilities, $\sim 1.0 \times 10^{-18} \text{ m}^2$, are found in the *Annweiler* unit (Fig. 11b). Permeability is plotted as a function of connected porosity in Fig. 12, and as a function of clay content and average grain diameter in Fig. 13 [we define “clay content” here as muscovite/illite–smectite (plus kaolinite for the Bust quarry sample); Tables 2, 3]. Our data show that permeability increases as porosity is increased (Fig. 12). Empirically, the data are best described by an exponential law (Fig. 12). Permeability appears to decrease with increasing clay content (Fig. 13a). In detail, samples containing a clay content lower than 4 wt% can have permeabilities as high as $\sim 10^{-13} \text{ m}^2$; samples containing a clay content of 5 wt% and above are characterised by lower permeabilities, from $\sim 10^{-18}$ to $\sim 10^{-16} \text{ m}^2$ (Fig. 13a). Permeability also appears to increase with increasing grain diameter (Fig. 13b). For example, samples with a grain diameter of $\sim 140 \mu\text{m}$ have permeabilities as low as $\sim 10^{-18} \text{ m}^2$ and samples with grain diameters between ~ 350 and $\sim 375 \mu\text{m}$ can have permeabilities as high as $\sim 10^{-13} \text{ m}^2$ (Fig. 13b). There are no obvious differences between parallel and perpendicular permeabilities for the uppermost (*Voltzia*, *Intermédiaires*, and *Karlstal*) and lowermost units (*Annweiler* and *Anté-Annweiler*). However, the mid-depth samples, from the *Rehberg* unit in particular (samples that contain high porosities; Fig. 11a), are noticeably more permeable when measured parallel to bedding (Fig. 11b). The ratio of permeability parallel and perpendicular to bedding is plotted as a function of connected porosity, clay content, and average grain diameter in Fig. 14. Five sandstones are measurably more permeable parallel to bedding: samples 84, 299, 347, 453, and 540. Notably, sample 347 is more than an order of magnitude more permeable when measured parallel to bedding. The ratio of permeability parallel and perpendicular to bedding does not appear to be related to connected porosity (Fig. 14a), clay content (Fig. 14b), or average grain diameter (Fig. 14c).

Table 4 Connected porosity, dry and wet *P*-wave velocities, and permeability for each of the prepared 20-mm-diameter samples

Sample	Depth (m)	Connected porosity	Dry <i>P</i> -wave velocity (km/s)	Wet <i>P</i> -wave velocity (km/s)	Permeability (m ²)
84-1 (perp)	1008	0.097	3.66	4.38	1.91×10^{-18}
84-2 (perp)	1008	0.096	3.69	4.43	2.69×10^{-18}
84-3 (perp)	1008	0.097	3.62	4.39	3.30×10^{-18}
84-4 (perp)	1008	0.093	3.79	4.46	2.64×10^{-18}
84-5 (perp)	1008	0.097	3.71	4.39	3.66×10^{-18}
84-6 (perp)	1008	0.094	3.79	4.47	1.59×10^{-18}
84-7 (perp)	1008	0.098	3.78	4.44	4.26×10^{-18}
84-8 (perp)	1008	0.094	3.80	4.51	2.46×10^{-18}
84-1 (para)	1008	0.074	4.46	4.92	8.58×10^{-18}
84-2 (para)	1008	0.076	4.51	4.90	8.61×10^{-18}
100-1 (perp)	1022	0.065	3.59	4.61	7.91×10^{-18}
100-2 (perp)	1022	0.066	3.56	4.59	7.53×10^{-18}
100-3 (perp)	1022	0.070	3.60	4.55	5.49×10^{-18}
100-4 (perp)	1022	0.064	3.72	4.66	4.83×10^{-18}
100-5 (perp)	1022	0.066	3.64	4.61	6.98×10^{-18}
100-6 (perp)	1022	0.063	3.71	4.65	5.92×10^{-18}
100-7 (perp)	1022	0.070	3.49	4.53	7.53×10^{-18}
100-8 (perp)	1022	0.061	3.78	4.71	5.38×10^{-18}
100-1 (para)	1022	0.067	4.05	4.59	6.21×10^{-18}
100-2 (para)	1022	0.067	4.01	4.62	6.95×10^{-18}
157-1 (perp)	1069	0.117	3.43	4.18	1.24×10^{-16}
157-2 (perp)	1069	0.120	3.35	4.11	1.56×10^{-16}
157-3 (perp)	1069	0.120	3.40	4.26	1.83×10^{-16}
157-4 (perp)	1069	0.117	3.39	4.30	1.41×10^{-16}
157-5 (perp)	1069	0.114	3.43	4.40	1.04×10^{-16}
157-6 (perp)	1069	0.118	3.33	4.28	1.68×10^{-16}
157-7 (perp)	1069	0.113	3.43	4.33	1.13×10^{-16}
157-8 (perp)	1069	0.108	3.41	4.27	7.64×10^{-17}
157-1 (para)	1069	0.133	3.68	4.03	1.86×10^{-16}
157-2 (para)	1069	0.086	4.58	4.81	6.21×10^{-17}
198-1 (perp)	1107	0.099	3.25	4.39	1.44×10^{-16}
198-2 (perp)	1107	0.096	3.23	4.43	1.18×10^{-16}
198-3 (perp)	1107	0.096	3.18	4.36	5.00×10^{-17}
198-4 (perp)	1107	0.097	3.20	4.35	4.39×10^{-17}
198-5 (perp)	1107	0.097	3.21	4.40	7.69×10^{-17}
198-6 (perp)	1107	0.099	3.24	4.36	4.53×10^{-17}
198-7 (perp)	1107	0.095	3.27	4.31	7.81×10^{-17}
198-1 (para)	1107	0.081	3.86	4.43	5.28×10^{-17}
198-2 (para)	1107	0.082	3.84	4.48	2.21×10^{-17}
248-1 (perp)	1151	0.143	3.13	4.10	4.15×10^{-15}
248-2 (perp)	1151	0.141	3.10	4.09	3.68×10^{-15}
248-3 (perp)	1151	0.143	3.05	4.09	4.52×10^{-15}
248-4 (perp)	1151	0.144	3.09	4.14	6.79×10^{-15}
248-5 (perp)	1151	0.148	3.14	4.09	8.06×10^{-15}
248-6 (perp)	1151	0.143	3.12	4.09	4.18×10^{-15}
248-7 (perp)	1151	0.145	3.11	4.06	6.08×10^{-15}
248-8 (perp)	1151	0.143	3.07	4.07	4.42×10^{-15}
248-1 (para)	1151	0.144	3.60	4.02	6.85×10^{-15}

Table 4 continued

Sample	Depth (m)	Connected porosity	Dry <i>P</i> -wave velocity (km/s)	Wet <i>P</i> -wave velocity (km/s)	Permeability (m ²)
248-2 (para)	1151	0.143	3.59	4.03	7.19×10^{-15}
299-1 (perp)	1197	0.130	3.40	4.16	9.22×10^{-18}
299-2 (perp)	1197	0.128	3.40	4.15	1.44×10^{-17}
299-3 (perp)	1197	0.131	3.33	4.14	1.64×10^{-17}
299-4 (perp)	1197	0.128	3.37	4.10	7.84×10^{-18}
299-5 (perp)	1197	0.130	3.40	4.14	8.42×10^{-18}
299-6 (perp)	1197	0.131	3.34	4.13	1.37×10^{-17}
299-7 (perp)	1197	0.127	3.37	4.11	1.07×10^{-17}
299-8 (perp)	1197	0.131	3.30	4.08	1.15×10^{-17}
299-1 (para)	1197	0.125	3.91	4.06	6.49×10^{-17}
299-2 (para)	1197	0.125	3.85	4.07	6.54×10^{-17}
347-1 (perp)	1239	0.184	2.87	3.88	3.04×10^{-15}
347-2 (perp)	1239	0.181	2.86	3.85	3.43×10^{-15}
347-3 (perp)	1239	0.185	2.94	3.81	4.51×10^{-15}
347-4 (perp)	1239	0.192	3.07	3.81	5.30×10^{-15}
347-5 (perp)	1239	0.185	2.86	3.88	5.74×10^{-15}
347-6 (perp)	1239	0.185	2.76	3.85	3.88×10^{-15}
347-7 (perp)	1239	0.182	2.86	3.82	6.70×10^{-15}
347-1 (para)	1239	0.190	3.16	3.64	1.29×10^{-13}
347-2 (para)	1239	0.184	3.19	3.69	7.30×10^{-14}
402-1 (perp)	1290	0.130	3.10	4.06	2.72×10^{-16}
402-2 (perp)	1290	0.131	3.11	4.08	2.72×10^{-16}
402-3 (perp)	1290	0.130	3.07	4.12	2.03×10^{-16}
402-4 (perp)	1290	0.131	3.04	4.07	2.09×10^{-16}
402-5 (perp)	1290	0.133	3.02	4.05	1.97×10^{-16}
402-6 (perp)	1290	0.132	3.05	4.06	2.56×10^{-16}
402-7 (perp)	1290	0.133	3.02	4.07	2.42×10^{-16}
402-8 (perp)	1290	0.131	3.05	4.05	2.43×10^{-16}
402-1 (para)	1290	0.134	3.52	3.99	4.35×10^{-16}
402-2 (para)	1290	0.134	3.56	4.01	4.59×10^{-16}
453-1 (perp)	1336	0.196	2.63	3.64	1.15×10^{-14}
453-2 (perp)	1336	0.192	2.65	3.64	9.79×10^{-15}
453-3 (perp)	1336	0.188	2.69	3.66	1.36×10^{-14}
453-4 (perp)	1336	0.189	2.68	3.69	8.63×10^{-15}
453-5 (perp)	1336	0.187	2.64	3.68	8.26×10^{-15}
453-6 (perp)	1336	0.189	2.66	3.67	7.90×10^{-15}
453-7 (perp)	1336	0.186	2.66	3.68	6.44×10^{-15}
453-8 (perp)	1336	0.184	2.65	3.71	6.37×10^{-15}
453-1 (para)	1336	0.181	2.99	3.54	3.11×10^{-14}
453-2 (para)	1336	0.178	3.05	3.55	2.33×10^{-14}
497-1 (perp)	1376	0.034	4.09	5.05	2.89×10^{-18}
497-2 (perp)	1376	0.036	4.13	5.15	1.95×10^{-18}
497-3 (perp)	1376	0.034	4.12	5.10	2.42×10^{-18}
497-4 (perp)	1376	0.032	4.09	5.09	1.39×10^{-18}
497-5 (perp)	1376	0.036	4.16	5.10	1.62×10^{-18}
497-6 (perp)	1376	0.034	4.18	5.09	1.73×10^{-18}
497-7 (perp)	1376	0.034	4.14	5.11	2.34×10^{-18}
497-8 (perp)	1376	0.032	4.04	5.08	2.31×10^{-18}
497-1 (para)	1376	0.033	4.53	5.17	8.36×10^{-19}

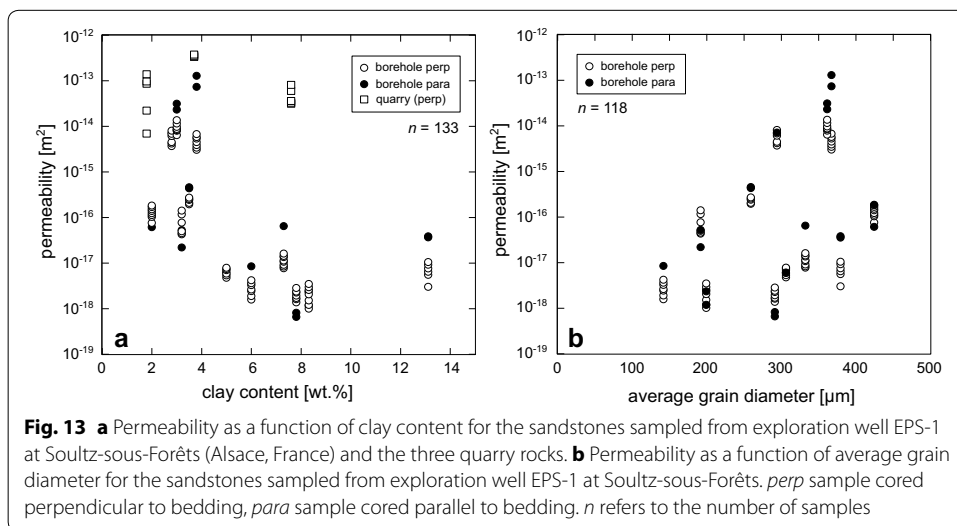
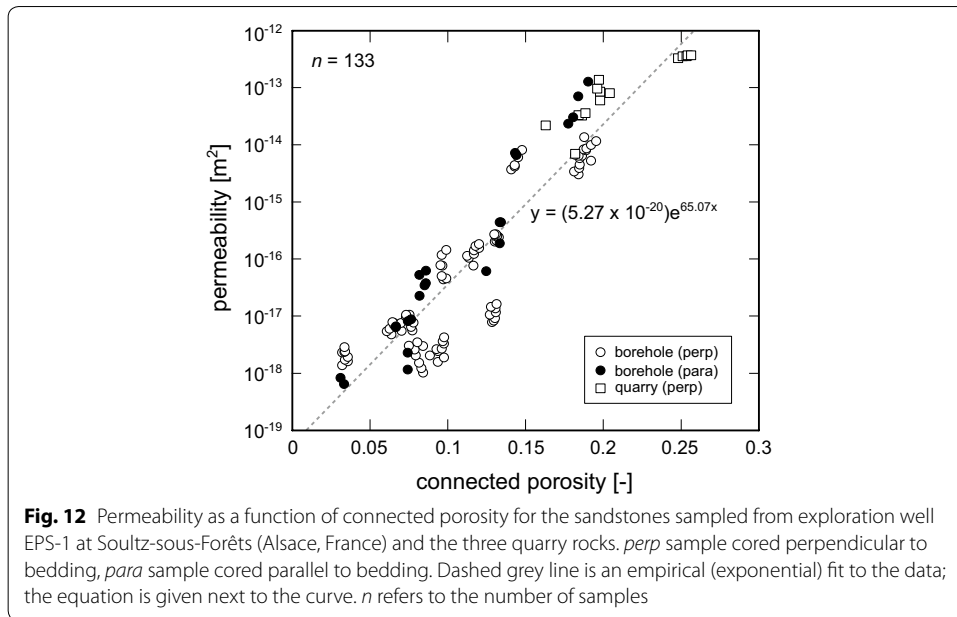
Table 4 continued

Sample	Depth (m)	Connected porosity	Dry <i>P</i> -wave velocity (km/s)	Wet <i>P</i> -wave velocity (km/s)	Permeability (m ²)
497-2 (para)	1376	0.034	4.55	5.17	6.70×10^{-19}
508-1 (perp)	1386	0.083	3.39	4.38	1.23×10^{-18}
508-2 (perp)	1386	0.080	3.41	4.41	3.53×10^{-18}
508-3 (perp)	1386	0.079	3.41	4.44	2.60×10^{-18}
508-4 (perp)	1386	0.084	3.34	4.35	2.96×10^{-18}
508-5 (perp)	1386	0.082	3.39	4.40	1.54×10^{-18}
508-6 (perp)	1386	0.079	3.44	4.43	2.05×10^{-18}
508-7 (perp)	1386	0.084	3.37	4.36	1.02×10^{-18}
508-8 (perp)	1386	0.088	3.35	4.34	2.07×10^{-18}
508-1 (para)	1386	0.075	3.95	4.45	1.18×10^{-18}
508-2 (para)	1386	0.074	3.94	4.45	2.37×10^{-18}
540-1 (perp)	1414	0.073	2.86	4.26	9.81×10^{-18}
540-2 (perp)	1414	0.076	2.84	4.24	1.06×10^{-17}
540-3 (perp)	1414	0.077	2.92	4.22	5.62×10^{-18}
540-4 (perp)	1414	0.075	2.88	4.22	3.07×10^{-18}
540-5 (perp)	1414	0.073	2.87	4.26	1.06×10^{-17}
540-6 (perp)	1414	0.078	2.83	4.18	7.69×10^{-18}
540-7 (perp)	1414	0.077	2.88	4.24	6.50×10^{-18}
540-8 (perp)	1414	0.075	2.84	4.28	9.31×10^{-18}
540-1 (para)	1414	0.085	3.48	4.43	3.53×10^{-17}
540-2 (para)	1414	0.086	3.58	4.32	3.84×10^{-17}
Bust-1 (perp)	Quarry	0.204	2.65	3.21	8.05×10^{-14}
Bust-2 (perp)	Quarry	0.186	2.72	3.23	3.21×10^{-14}
Bust-3 (perp)	Quarry	0.184	2.81	3.26	3.30×10^{-14}
Bust-4 (perp)	Quarry	0.198	2.77	3.27	5.95×10^{-14}
Bust-5 (perp)	Quarry	0.188	2.80	3.27	3.57×10^{-14}
Rothbach-1 (perp)	Quarry	0.182	3.50	3.95	2.19×10^{-14}
Rothbach-2 (perp)	Quarry	0.196	3.38	3.83	9.57×10^{-14}
Rothbach-3 (perp)	Quarry	0.182	3.47	3.93	6.93×10^{-15}
Rothbach-4 (perp)	Quarry	0.197	3.35	3.79	1.37×10^{-13}
Rothbach-5 (perp)	Quarry	0.198	3.44	3.80	8.53×10^{-14}
Adamswiller-1 (perp)	Quarry	0.253	2.29	3.04	3.51×10^{-13}
Adamswiller-2 (perp)	Quarry	0.251	2.30	3.08	3.53×10^{-13}
Adamswiller-3 (perp)	Quarry	0.254	2.35	3.05	3.66×10^{-13}
Adamswiller-4 (perp)	Quarry	0.256	2.34	2.96	3.70×10^{-13}
Adamswiller-5 (perp)	Quarry	0.248	2.32	3.06	2.28×10^{-13}

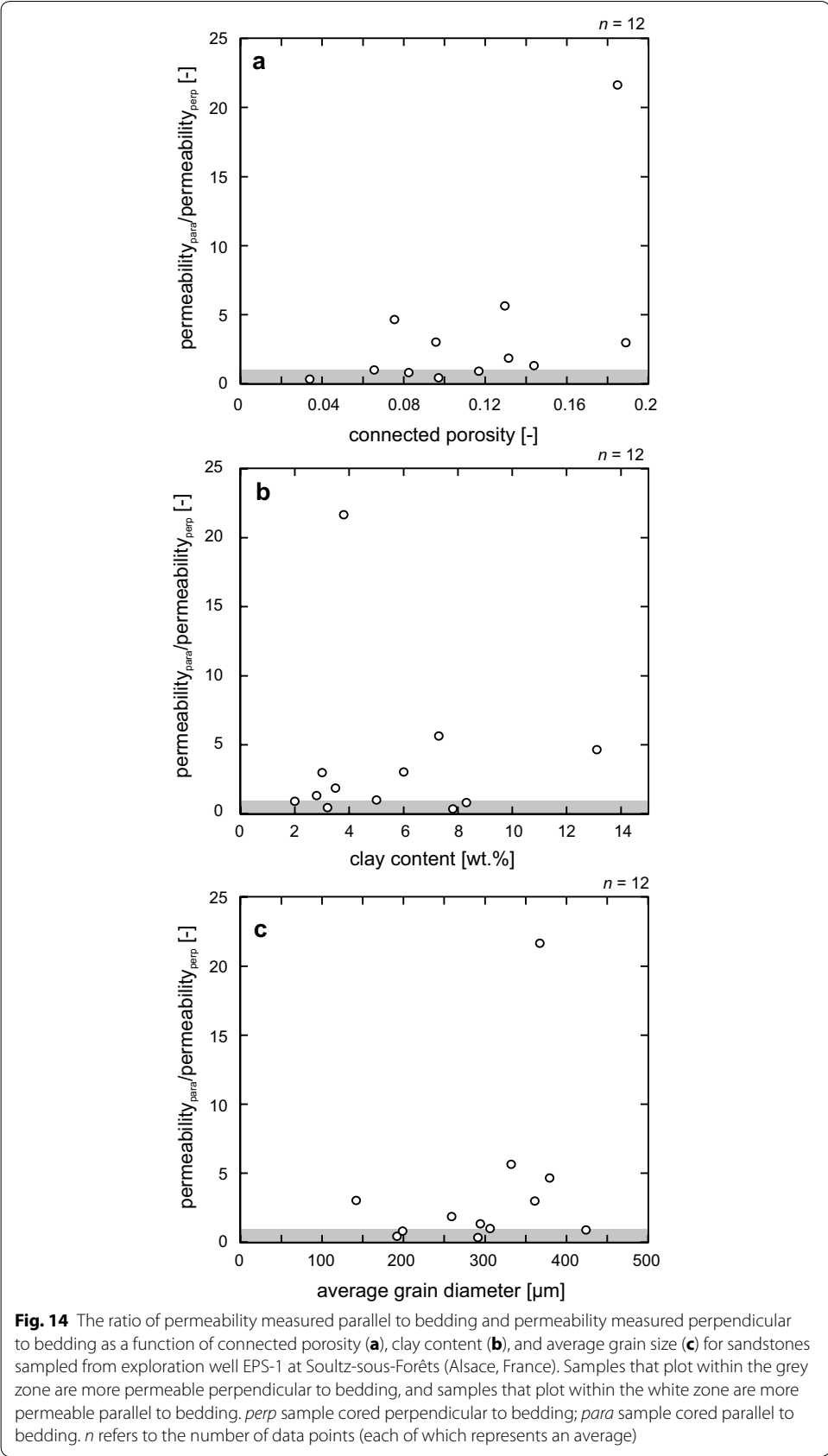
perp sample cored perpendicular to bedding; *para* sample cored parallel to bedding

The sample numbers refer to their box number

Figure 11c shows that *P*-wave velocities decrease with depth down to the base of the *Trifels* unit at a depth of ~ 1350 m. *P*-wave velocities are higher for the samples from the *Annweiler* unit, but are low in the *Anté-Annweiler* unit (Fig. 11c). *P*-wave velocity is plotted as a function of connected porosity and clay content in Fig. 15. *P*-wave velocity decreases as porosity is increased (Fig. 15a), but appears unrelated to clay content



(Fig. 15b). Dry *P*-wave velocities measured on the borehole samples parallel to bedding (black circles in Fig. 15a) are consistently higher (by about 10–25%, see Fig. 16a, b) than those measured on the borehole samples prepared perpendicular to bedding (white circles in Fig. 15a), although this increase appears unrelated to porosity (Fig. 16a) and clay content (Fig. 16b). Wet *P*-wave velocities (blue and purple circles and blue squares in Fig. 15a) are consistently higher than dry *P*-wave velocities (white and black circles and white squares in Fig. 15a). In detail, saturation with water increases the *P*-wave velocity of the samples cored perpendicular and parallel to bedding by about 20–50 and 5–20%, respectively (Fig. 16c, d). However, *P*-wave velocity increases due to water saturation do not vary as a function of either porosity (Fig. 16c) or clay content (Fig. 16d). The



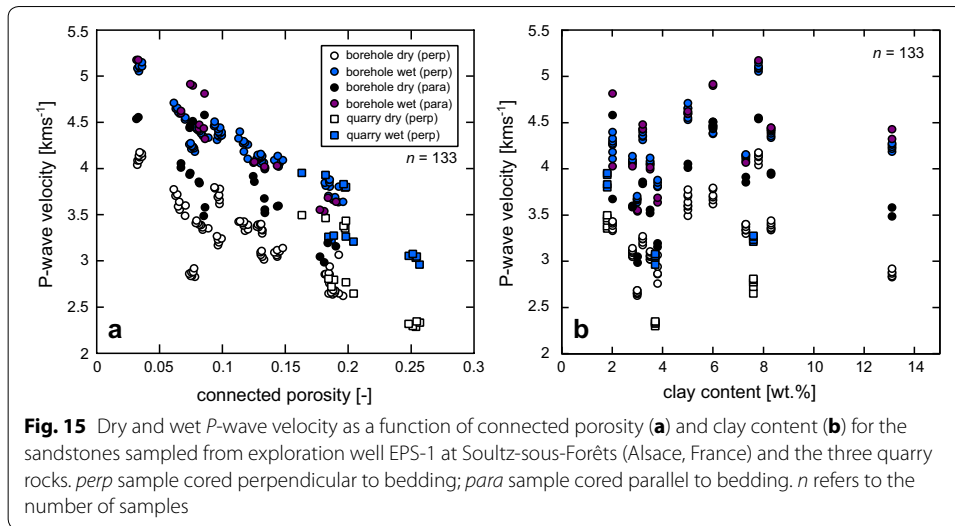


Fig. 15 Dry and wet *P*-wave velocity as a function of connected porosity (a) and clay content (b) for the sandstones sampled from exploration well EPS-1 at Soultz-sous-Forêts (Alsace, France) and the three quarry rocks. *perp* sample cored perpendicular to bedding; *para* sample cored parallel to bedding. *n* refers to the number of samples

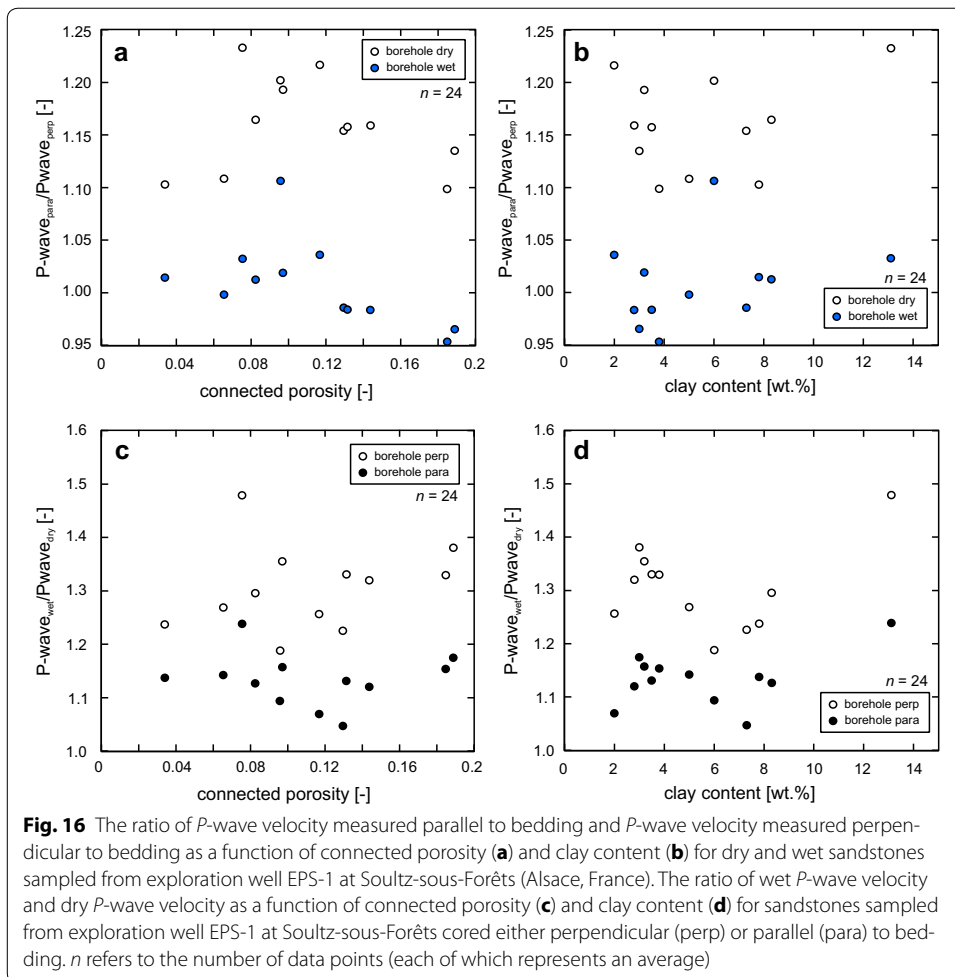


Fig. 16 The ratio of *P*-wave velocity measured parallel to bedding and *P*-wave velocity measured perpendicular to bedding as a function of connected porosity (a) and clay content (b) for dry and wet sandstones sampled from exploration well EPS-1 at Soultz-sous-Forêts (Alsace, France). The ratio of wet *P*-wave velocity and dry *P*-wave velocity as a function of connected porosity (c) and clay content (d) for sandstones sampled from exploration well EPS-1 at Soultz-sous-Forêts cored either perpendicular (*perp*) or parallel (*para*) to bedding. *n* refers to the number of data points (each of which represents an average)

difference in water-saturated *P*-wave velocity between the perpendicular and parallel samples is negligible (Fig. 15a).

Discussion

Matrix permeability of the Buntsandstein

Our data show that the permeability of the Buntsandstein sandstones increases as porosity is increased (Fig. 12), in accordance with previous studies on sandstones (e.g. Bourbié and Zinszner 1985; Nelson 1994; Wadsworth et al. 2016). We find that the matrix permeability of the Buntsandstein sandstone ranges from $\sim 10^{-18}$ to $\sim 10^{-13}$ m² (Fig. 12). Our permeability data are in agreement with recently published permeability data for Buntsandstein sandstones from EPS-1 (Griffiths et al. 2016; Fig. 17). However, we highlight that permeability measurements of the EPS-1 cores performed using a TinyPerm II field permeameter suggest that the permeability of the Buntsandstein varies from $\sim 10^{-15}$ to $\sim 10^{-12}$ m² (Haffen et al. 2013), much higher than the values measured herein and by Griffiths et al. (2016). We note that the lowest permeability measurable using the TinyPerm II is 6.92×10^{-16} m² (Farquharson et al. 2015), highlighting that the TinyPerm II field permeameter may not be an appropriate tool for measuring the permeability of several units of the Buntsandstein, especially the *Voltzia*, *Annweiler*, and *Anté-Annweiler* units (Fig. 11b).

Our data also highlight that five of the sandstones are more permeable when measured parallel to bedding than in the perpendicular direction (Fig. 14). The permeability of these samples is between a factor of three to five higher parallel to bedding in samples 84, 299, 453, and 540, and more than an order of magnitude higher in sample 347 (Fig. 14). Permeability measured parallel and perpendicular to bedding is very similar for the remaining samples (Fig. 14). The data of Griffiths et al. (2016) also highlight a permeability anisotropy within the Buntsandstein. For example, a sandstone from the

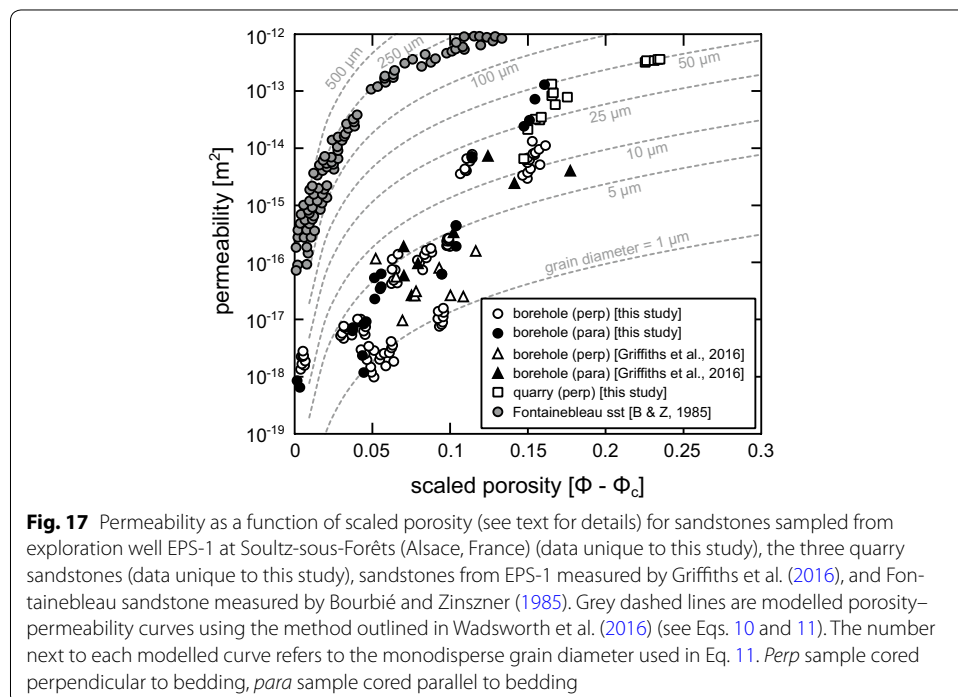


Fig. 17 Permeability as a function of scaled porosity (see text for details) for sandstones sampled from exploration well EPS-1 at Soultz-sous-Forêts (Alsace, France) (data unique to this study), the three quarry sandstones (data unique to this study), sandstones from EPS-1 measured by Griffiths et al. (2016), and Fontainebleau sandstone measured by Bourbié and Zinszner (1985). Grey dashed lines are modelled porosity–permeability curves using the method outlined in Wadsworth et al. (2016) (see Eqs. 10 and 11). The number next to each modelled curve refers to the monodisperse grain diameter used in Eq. 11. *Perp* sample cored perpendicular to bedding, *para* sample cored parallel to bedding

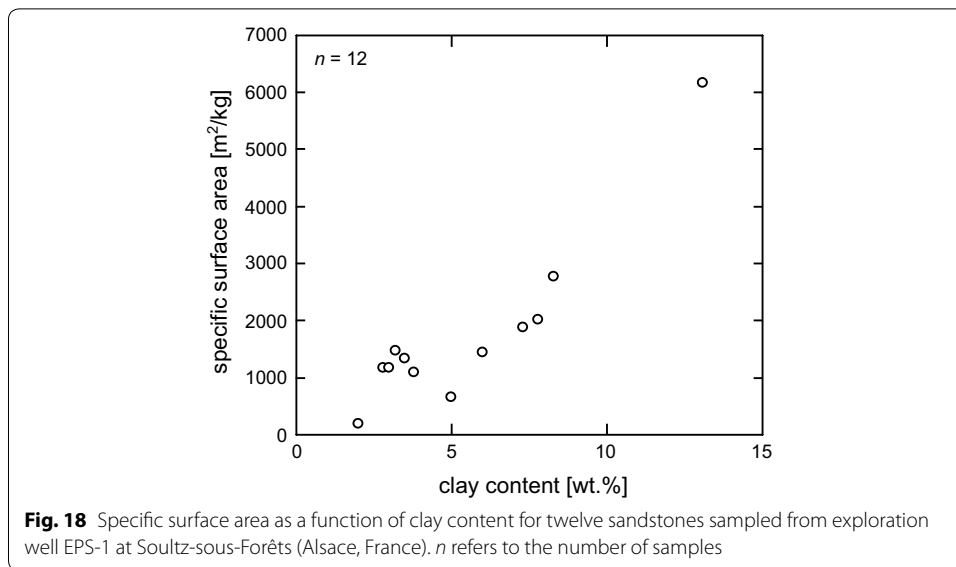
Karlstal unit (depth = 1083 m) was about two orders of magnitude more permeable when measured parallel to bedding (Griffiths et al. 2016). However, understanding why some samples are more permeable parallel to bedding, whilst others are not, is difficult to reconcile: permeability anisotropy is not related to connected porosity, clay content, or average grain size (Fig. 14). Further, of the five samples that show permeability anisotropy, some are homogenous (microscopically and on the sample length scale) (samples 84, 347, and 453; Fig. 8), whilst others are layered/laminated (299 and 540; Fig. 8). To emphasise, the sample that contains the most obvious laminations—sample 497 (Fig. 2j)—is marginally less permeable when oriented parallel to bedding (Table 4).

Since the grains in sandstones are typically orientated such that their pore major axis is sub-parallel to bedding (Louis et al. 2003; Benson et al. 2005; Robion et al. 2014; Griffiths et al. 2017; Farrell and Healy 2017), a higher permeability parallel to bedding is perhaps expected. Although we do not provide an average orientation for the pore or grain major axes of the Buntsandstein sandstones studied herein, we do note that their average grain aspect ratios are within the range 1.54–1.76 (Table 1). Higher permeabilities parallel to bedding, compared to measurements performed on samples prepared perpendicular to bedding, have been previously reported by Bell and Culshaw (1998). These authors showed that the permeability of sandstones (from the Sneinton Formation in England) with a range of connected porosity (from 0.09 to 0.14) was ~ 40 to 60% higher when measured parallel to bedding (Bell and Culshaw 1998). Farrell et al. (2014) and Farrell and Healy (2017) also show that pore elongation through cataclasis and shearing can create a permeability anisotropy adjacent to faults in porous sandstone. However, data from Benson et al. (2005) show a permeability anisotropy in low-porosity (porosity = 0.04) Crab Orchard sandstone, but no permeability anisotropy in high-porosity (porosity = 0.23) Bentheim sandstone. As mentioned above, we only observed a substantial permeability anisotropy in one of the high-porosity samples (Fig. 14). We suggest that the absence of a permeability anisotropy in the sandstones of the Buntsandstein is likely a result of abundant pore-filling minerals found in these sandstones (Figs. 8, 9, and 10). The presence/absence of a permeability anisotropy in sandstone is likely therefore related to the shape of the grains (Table 1), a factor that dictates the shape of the pores (the inter-grain voids), and the nature and extent of pore-filling minerals.

If we compare our data with those from Bourbié and Zinszner (1985), who measured the permeability of a suite of variably porous Fontainebleau sandstone (99% quartz and clay-free), we find that the permeability of the Buntsandstein sandstones is up to four or five orders of magnitude lower for a given porosity (Fig. 17). To explore this difference further, we provide modelled porosity–permeability curves for granular materials with different monodisperse grain diameters. Permeability is modelled using the following relation (Martys et al. 1994; Wadsworth et al. 2016):

$$k_D = \frac{2\phi}{s^2} (\phi - \phi_c)^b, \quad (11)$$

where s is the specific surface, ϕ_c is the porosity at the percolation threshold (taken here to be 0.03; Wadsworth et al. 2016), $\phi_* = 1 - (\phi - \phi_c)$, and b is a constant related to the initial particle geometry (taken here to be 4.2; see Wadsworth et al. 2016). Although we can model the permeability using our specific surface areas (Table 1), we note that

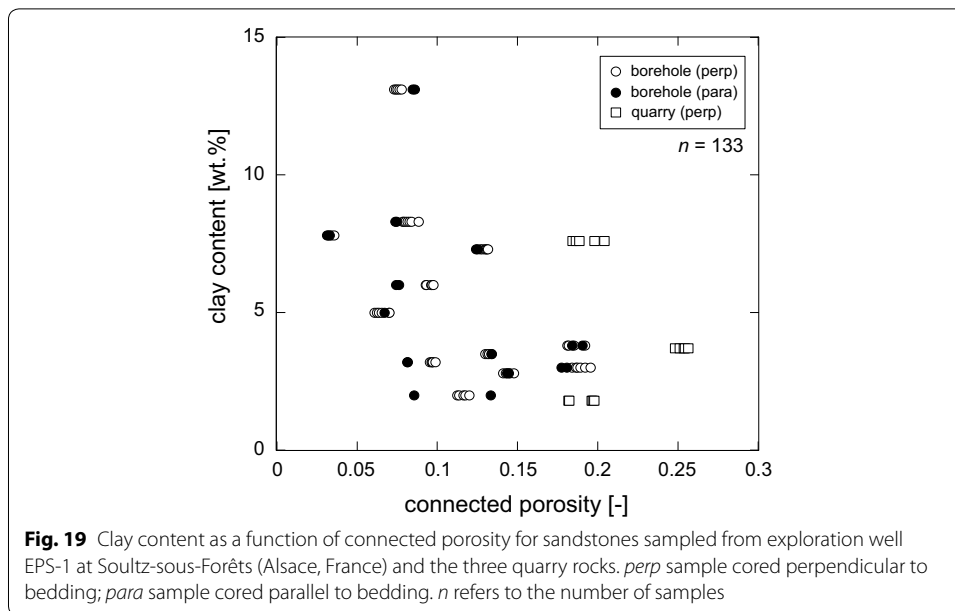


they are anomalously high as a result of the high clay content of these materials (Fig. 4; Table 2). Clay minerals have a high specific surface area due to their plate-like structure; indeed, specific surface area increases as clay content is increased (Fig. 18). Instead, for an initial non-overlapping, monodisperse grain radius R , we can compute an “effective” pore radius a and therefore the evolution of the specific surface during porosity reduction using the following relation [see Wadsworth et al. (2016) for the calculation of a]:

$$s(a) = \frac{3(1 - \phi)\ln(1 - \phi)}{a}. \tag{12}$$

Using Eqs. (11) and (12), we provide modelled porosity–permeability curves for a range of grain diameters ($2R$) from 1 μm up to 500 μm in Fig. 17. We first note that the model provides an excellent description of the permeability of Fontainebleau sandstone, which has a grain diameter of 250 μm (David et al. 1994). The model predicts grain diameters between 1 and 50 μm for the Buntsandstein sandstones (Fig. 17). However, these predicted grain diameters are considerably smaller than the measured grain diameters (Table 1; Fig. 6), although we note that permeability still appears to be correlated with average grain diameter (Fig. 13b). We interpret the discrepancy between the permeability of the Buntsandstein sandstones and the Fontainebleau sandstone data and model predictions as a result of the abundant pore-filling minerals in the Buntsandstein sandstones (Figs. 8, 9, and 10), as concluded by Griffiths et al. (2016).

We find that permeability appears to decrease as clay content increases (Fig. 13a). However, although high clay contents are typically associated with low permeabilities, we highlight here that porosity also varies with clay content (Fig. 19). The trend seen in Fig. 13a could therefore be explained by the relationship between porosity and clay content. We further note that the permeability measurements presented herein were measured using inert gas as the pore fluid. Permeability to water will likely be lower than the gas permeabilities provided herein due to the presence of swelling clays (although



we note that only 5–6% of the clays are smectite) (Davy et al. 2007; Faulkner and Rutter 2000; Tanikawa and Shimamoto 2006, 2009). The relationship between permeability and clay content may also be more pronounced if water was used as the pore fluid.

***P*-wave velocity of the Buntsandstein**

Our data show that the *P*-wave velocity of the Buntsandstein decreases as porosity is increased (Fig. 15a), in accordance with previous studies (e.g. Han et al. 1986; Eberhart-Phillips et al. 1989). The studies of Han et al. (1986) and Eberhart-Phillips et al. (1989) also demonstrate that *P*-wave velocity depends on clay content. However, the empirical equations provided by these studies—that relate permeability to porosity and clay content—overestimate the *P*-wave velocity of the materials studied herein. This difference may be due to (1) the higher confining pressures used in the experiments of Han et al. (1986) and Eberhart-Phillips et al. (1989) and/or (2) the fact that the clays within the Buntsandstein sandstones are present as pore-filling minerals (Figs. 8, 9, 10). Indeed, clay content does not appear to exert a dominant control on *P*-wave velocity (Fig. 15b).

Our data also show that *P*-wave velocities parallel to bedding are higher than those measured perpendicular to bedding, and that water saturation increases *P*-wave velocity (Figs. 15, 16). Previous measurements on sandstones show that *P*-wave velocity is faster parallel to bedding (e.g. Benson et al. 2005). Since the grain major axis is typically sub-parallel to bedding in sandstones, elastic waves travelling perpendicular to bedding will encounter more grain-to-grain interfaces, which will reduce the elastic wave velocity. Such *P*-wave anisotropy in clay rich rocks, such as shale, has also been attributed to preferential clay alignment in the direction of bedding (Johnston and Christensen 1995). However, since the clay minerals in the Buntsandstein sandstones from EPS-1 are present as pore-filling (e.g. Fig. 9b, c, f, l) or pore-lining minerals (e.g. Figs 9k, 10b, e, d), it is unlikely that they are oriented with respect to bedding. This could explain why the ratio of parallel to perpendicular *P*-wave velocity is uninfluenced by clay content (Fig. 16b).

We also find that P -wave velocity is increased upon saturation with water (Figs. 15, 16). Previously published measurements also show that the P -wave velocity of sandstone increases upon saturation with water (e.g. Zang et al. 1996; Zamora and Poirier 1990; Louis et al. 2003; Kahraman 2007) and is simply a consequence of the fact that P -waves travel faster through water than through air.

Geothermal implications and concluding remarks

Our new laboratory data show that the matrix permeabilities of the Buntsandstein sandstones from EPS-1 are low (Table 4; Figs. 11b, 12, 17) due to the filling or partial filling of pores with clays (illite–smectite), dolomite, siderite, and barite (Figs. 8, 9, and 10). The lowest permeabilities—as low as $\sim 1.0 \times 10^{-18} \text{ m}^2$ —are found in the rocks that form the transition zone between the granite and the Buntsandstein, namely the *Annweiler* and *Anté-Annweiler* units, and the *Voltzia* unit at the Buntsandstein–Muschelkalk interface (Fig. 11b). It is important to note that measurements of matrix permeability in the laboratory do not take meso- and macroscale fractures into account (see Heap and Kennedy 2016), which are abundant in the Buntsandstein (Nollet et al. 2009; Haffen et al. 2013; Vidal et al. 2015; Griffiths et al. 2016). Indeed, the Buntsandstein contains several permeable fracture zones that control the top of the convection cells (Vidal et al. 2015). As a result, the permeability data presented herein should be considered as a lower boundary for permeability in the Buntsandstein units of the Upper Rhine Graben. Since numerical modelling suggests that the equivalent permeability of the reservoir and overlying sediments needs to be $\sim 10^{-14} \text{ m}^2$ to support the regional hydrothermal convection cells (Magenet et al. 2014), the data of this study therefore highlight the importance of meso- and macroscale fractures in raising the equivalent permeability of the system to a value sufficient to maintain the hydrothermal circulation. Indeed, the low-permeability *Annweiler* unit contains a high fracture density of 2.14 fractures/m (the mean fracture density of the Buntsandstein is 0.81 fractures/m) (Haffen et al. 2013). However, in zones of high matrix permeability (Fig. 11b) and low fracture density (Haffen et al. 2013), such as the *Karlstal* unit, matrix permeability may be important for large-scale, bedding-parallel fluid flow (Haffen et al. 2013). Higher permeability parallel to bedding, as measured for five of the twelve Buntsandstein sandstones (Fig. 14), may also enhance bedding-parallel fluid flow in layers with a low fracture density.

Estimations of the timescales of fracture-filling precipitation highlight that a two-mm-wide fracture within the Buntsandstein can effectively seal, thus greatly reducing equivalent permeability, within 1 month (Griffiths et al. 2016). A recent experimental study has shown that the permeability of a porous sandstone can be reduced by up to an order of magnitude following 24 h of continuous flow of a Ba-rich fluid through the sample, due to the precipitation of barite within pores (Orywall et al. 2017). Therefore, we highlight that fracturing or slip on pre-existing fractures—through natural tectonic deformation or anthropogenic stimulation (e.g. Audigane et al. 2002; Evans et al. 2005; Evans 2005; Lengliné et al. 2017)—must outperform fracture sealing to maintain the permeability required for geothermal circulation in the Upper Rhine Graben.

We have also shown that the sandstones of the Buntsandstein exhibit a P -wave anisotropy and that water saturation greatly increases their P -wave velocity (Figs. 15, 16). Interestingly, saturation with water effectively removes the P -wave anisotropy (Figs. 15,

16; Table 4). The P -wave velocity data presented herein may therefore help guide future seismic investigations at geothermal sites within the Upper Rhine Graben (e.g. Beauce et al. 1991, 1995; Moriya et al. 2003; Bourouis and Bernard 2007; Sausse et al. 2010; Place et al. 2010; Lengliné et al. 2017).

Abbreviations and symbols

EGS: enhanced geothermal system; XRPD: X-ray powder diffraction; BET: Brunauer–Emmet–Teller; SEM: scanning electron microscope; BSE: backscattered scanning electron microscope; l_{major} : length of the major axis of the best-fit ellipse; l_{minor} : length of the minor axis of the best-fit ellipse; g_d : area of a grain; g_p : perimeter of a grain; \bar{d} : average grain diameter; EDS: energy-dispersive X-ray spectroscopy; P_c : confining pressure; Q_v : volumetric flow rate; ΔP : pressure gradient (upstream pore fluid pressure minus downstream pore fluid pressure); P_u : upstream pore fluid pressure; P_d : downstream pore fluid pressure; k_D : Darcian permeability; P_m : mean pore fluid pressure; μ : pore fluid viscosity; L : sample length; A : sample cross-sectional area; k_{Forch} : Forchheimer-corrected permeability; ξ : constant; slope of the plot of the reciprocal of the Darcian permeability as a function of the volumetric flow rate; k_{link} : Klinkenberg-corrected permeability; P_f : final, equilibrated pore fluid pressure across the sample; t : time; V_u : volume of the upstream reservoir; V_d : volume of the downstream reservoir; α : constant; slope of the graph of $\log(P_u - P_f)$ as a function of time; β : compressibility of the pore fluid pressure; P_{eff} : effective pressure (confining pressure minus the pore fluid pressure); q_v : volumetric gas flux; x : distance along the sample axis; P : gas pressure; Q_M : mass flow rate; m : mass of gas; V : volume of gas; M : molar mass of gas; R : ideal gas constant; T : temperature; ρ : gas density; Q_{V_i} : volumetric flow rate at the entrance of the sample; Q_{V_d} : volumetric flow rate at the exit of the sample; ϕ : sample porosity; s : specific surface; ϕ_c : porosity at the percolation threshold; b : constant related to the initial particle geometry; a : effective pore radius.

Authors' contributions

MJH led the project and wrote the manuscript. PB, MJH, and ARLK chose and collected the samples from the Merkwiller core repository. ARLK and MJH performed the porosity, permeability, and P -wave velocity measurements. HAG performed and interpreted the XRPD data. FBW performed the TG analysis. TR performed and interpreted the BET data. MJ Heap performed the grain size and shape analysis. All authors had a hand in the preparation of the manuscript and the interpretation of the data. All authors read and approved the final manuscript.

Author details

¹ Géophysique Expérimentale, Institut de Physique de Globe de Strasbourg (UMR 7516, CNRS, Université de Strasbourg/EOST), 5 rue René Descartes, 67084 Strasbourg Cedex, France. ² Lehrstuhl für Ingenieurgeologie, Technische Universität München, Arcisstr. 21, 80333 Munich, Germany. ³ Earth & Environmental Sciences, Ludwig Maximilians Universität, Theresienstr. 41/III, 80333 Munich, Germany.

Acknowledgements

We wish to thank Chrystal Dezayes, Gilles Morvan, Bertrand Renaudié, Coralie Aichholzer, Philippe Düringer, Jamie Farquharson, Luke Griffiths, Dave Healy, and Colin Taylor. The comments of two anonymous reviewers helped improve this manuscript.

Competing interests

The authors declare that they have no competing interests.

Availability of data and materials

The majority of data presented in this study are available in Tables 1, 2, 3, and 4. Other data could be made available upon request to the first author. Materials (samples, thin sections, etc.) could also be made available upon request to the first author.

Ethics approval and consent to participate

Not applicable.

Funding

This study was funded by LABEX grant ANR-11-LABX-0050_G-EAU-THERMIE-PROFONDE (this research therefore benefited from state funding managed by the Agence Nationale de la Recherche (ANR) as part of the "Investissements d'avenir" program) and ANR Grant CANTARE (ANR-15-CE06-0014-01).

Publisher's Note

Springer Nature remains neutral with regard to jurisdictional claims in published maps and institutional affiliations.

Received: 18 September 2017 Accepted: 15 November 2017

Published online: 21 November 2017

References

Aichholzer C, Düringer P, Orciani S, Genter A. New stratigraphic interpretation of the Soultz-sous-Forêts 30-year-old geothermal wells calibrated on the recent one from Rittershoffen (Upper Rhine Graben, France). *Geotherm Energy*. 2016;4(1):13.

- Audigane P, Royer JJ, Kaieda H. Permeability characterization of the Soultz and Ogachi large-scale reservoir using induced microseismicity. *Geophysics*. 2002;67(1):204–11.
- Aquilina L, Pauwels H, Genter A, Fouillac C. Water-rock interaction processes in the Triassic sandstone and the granitic basement of the Rhine Graben: Geochemical investigation of a geothermal reservoir. *Geochimica et cosmochimica acta* 1997;61(20):4281–95.
- Baillieux P, Schill E, Edel JB, Mauri G. Localization of temperature anomalies in the Upper Rhine Graben: insights from geophysics and neotectonic activity. *Int Geol Rev*. 2013;55(14):1744–62.
- Baria R, Baumgärtner J, Gérard A, Jung R, Garnish J. European HDR research programme at Soultz-sous-Forêts (France) 1987–1996. *Geothermics*. 1999;28(4):655–69.
- Baud P, Klein E, TfWong. Compaction localization in porous sandstones: spatial evolution of damage and acoustic emission activity. *J Struct Geol*. 2004;26(4):603–24.
- Baud P, Louis L, David C, Rawling GC, TfWong. Effects of bedding and foliation on mechanical anisotropy, damage evolution and failure mode. *Geol Soc Lond Spec Publ*. 2005;245(1):223–49.
- Baud P, Vajdova V, TfWong. Shear-enhanced compaction and strain localization: inelastic deformation and constitutive modeling of four porous sandstones. *J Geophys Res*. 2006;111(B12):1.
- Baujard C, Genter A, Dalmais E, Maurer V, Hehn R, Rosillette R, Vidal J, Schmittbuhl J. Hydrothermal characterization of wells GRT-1 and GRT-2 in Rittershoffen, France: implications on the understanding of natural flow systems in the Rhine graben. *Geothermics*. 2017;65:255–68.
- Beauce A, Fabriol H, Le Masne D, Cavoit C, Mechler P, Chen XK. Seismic studies on the HDR site of Soultz-sous-Forêts (Alsace, France). *Geotherm Sci Technol*. 1991;3(1–4):239–66.
- Beauce A, Jones R, Fabriol H, Hulot C. Seismic studies on the Soultz HDR project (France) during phase IIa. *Geotherm Sci Technol*. 1995;4(4):253–72.
- Bell FG, Culshaw MG. Petrographic and engineering properties of sandstones from the Sneinton Formation, Nottinghamshire, England. *Q J Eng Geol Hydrogeol*. 1998;31(1):5–19.
- Benson PM, Meredith PG, Platzman ES, White RE. Pore fabric anisotropy in porous sandstones and its relation to elastic wave velocity and permeability anisotropy under hydrostatic pressure. *Int J Rock Mech Min Sci*. 2005;42(7):890–9.
- Bergmann J, Friedel P, Kleeberg R. BGMN—a new fundamental parameters based Rietveld program for laboratory X-ray sources, its use in quantitative analysis and structure investigations. *CPD Newslett*. 1998;20(5):5.
- Bésuelle P, Baud P, TfWong. Failure mode and spatial distribution of damage in Rothbach sandstone in the brittle-ductile transition. *Pure Appl Geophys*. 2003;160(5):851–68.
- Bourbié T, Zinszner B. Hydraulic and acoustic properties as a function of porosity in Fontainebleau sandstone. *J Geophys Res*. 1985;90(B13):11524–32.
- Bourouis S, Bernard P. Evidence for coupled seismic and aseismic fault slip during water injection in the geothermal site of Soultz (France), and implications for seismogenic transients. *Geophys J Int*. 2007;169(2):723–32.
- Brace W, Walsh JB, Frangos WT. Permeability of granite under high pressure. *J Geophys Res*. 1968;73(6):2225–36.
- Buchmann TJ, Connolly PT. Contemporary kinematics of the Upper Rhine Graben: a 3D finite element approach. *Glob Planet Change*. 2007;58(1):287–309.
- David C, TfWong, Zhu W, Zhang J. Laboratory measurement of compaction-induced permeability change in porous rocks: implications for the generation and maintenance of pore pressure excess in the crust. *Pure Appl Geophys*. 1994;143(1–3):425–56.
- Davy CA, Skoczylas F, Barnichon JD, Lebon P. Permeability of macro-cracked argillite under confinement: gas and water testing. *Phys Chem Earth Parts A/B/C*. 2007;32(8):667–80.
- Dezayes C, Genter A, Valley B. Structure of the low permeable naturally fractured geothermal reservoir at Soultz. *CR Geosci*. 2010;342(7):517–30.
- Earnest CM. Thermal analysis of selected illite and smectite clay minerals. Part I. Illite clay specimens. In: *Thermal analysis in the Geosciences*. Berlin: Springer; 1991a.
- Earnest CM. Thermal analysis of selected illite and smectite clay minerals. Part II. Smectite clay minerals. In: *Thermal analysis in the Geosciences*. Berlin: Springer; 1991b.
- Eberhart-Phillips D, Han DH, Zoback MD. Empirical relationships among seismic velocity, effective pressure, porosity, and clay content in sandstone. *Geophysics*. 1989;54(1):82–9.
- Evans KF, Genter A, Sausse J. Permeability creation and damage due to massive fluid injections into granite at 3.5 km at Soultz: 1. Borehole observations. *J Geophys Res*. 2005;110(B4):B04203.
- Evans KF. Permeability creation and damage due to massive fluid injections into granite at 3.5 km at Soultz: 2. Critical stress and fracture strength. *J Geophys Res*. 2005;110(B4):B04203.
- Farrell NJC, Healy D, Taylor CW. Anisotropy of permeability in faulted porous sandstones. *J Struct Geol*. 2014;63:50–67.
- Farrell NJC, Healy D. Anisotropic pore fabrics in faulted porous sandstones. *J Struct Geol*. 2017;104:125–41.
- Farquharson JI, Heap MJ, Varley NR, Baud P, Reuschlé T. Permeability and porosity relationships of edifice-forming andesites: a combined field and laboratory study. *J Volcanol Geotherm Res*. 2015;297:52–68.
- Farquharson JI, Heap MJ, Lavallée Y, Varley NR, Baud P. Evidence for the development of permeability anisotropy in lava domes and volcanic conduits. *J Volcanol Geotherm Res*. 2016;323:163–85.
- Faulkner DR, Rutter EH. Comparisons of water and argon permeability in natural clay-bearing fault gouge under high pressure 20°C. *J Geophys Res*. 2000;105(B7):16415–26.
- Forchheimer PH. Wasserbewegung durch boden. *Zeit Ver Duetch Ing*. 1901;45:1782–8.
- Fuss S, Canadell JG, Peters GP, Tavoni M, Andrew RM, Ciais P, Jackson RB, Jones CD, Kraxner F, Nakicenovic N, Le Quéré C, Raupach R, Sharifi A, Smith P, Yamagata Y. Betting on negative emissions. *Nat Clim Change*. 2014;4(10):850–3.
- Genter A, Traineau H. Analysis of macroscopic fractures in granite in the HDR geothermal well EPS-1, Soultz-sous-Forêts, France. *J Volcanol Geotherm Res*. 1996;72(1–2):121–41.
- Gérard A, Kappelmeyer O. The Soultz-sous-Forêts project. *Geothermics*. 1987;16(4):393–9.
- Gérard A, Genter A, Kohl T, Lutz P, Rose P, Rummel F. The deep EGS (enhanced geothermal system) project at Soultz-sous-Forêts (Alsace, France). *Geothermics*. 2006;5(35):473–83.

- Guillou-Frottier L, Carré C, Bourguin B, Bouchot V, Genter A. Structure of hydrothermal convection in the Upper Rhine Graben as inferred from corrected temperature data and basin-scale numerical models. *J Volcanol Geotherm Res.* 2013;256:29–49.
- Griffiths L, Heap MJ, Wang F, Daval D, Gilg HA, Baud P, Schmittbuhl J, Genter A. Geothermal implications for fracture-filling hydrothermal precipitation. *Geothermics.* 2016;64:235–45.
- Griffiths L, Heap MJ, Xu T, Chen CF, Baud P. The influence of pore geometry and orientation on the strength and stiffness of porous rock. *J Struct Geol.* 2017;96:149–60.
- Haffen S, Géraud Y, Diraison M, Dezayes C. Fluid-flow zones in a geothermal sandstone reservoir: localization from thermal conductivity and temperature logs. *Geothermics.* 2013;46:32–41.
- Han DH, Nur A, Morgan D. Effects of porosity and clay content on wave velocities in sandstones. *Geophysics.* 1986;51(11):2093–107.
- Heap MJ, Kennedy BM. Exploring the scale-dependent permeability of fractured andesite. *Earth Planet Sci Lett.* 2016;447:139–50.
- Johnston JE, Christensen NI. Seismic anisotropy of shales. *J Geophys Res.* 1995;100(B4):5991–6003.
- Kahraman S. The correlations between the saturated and dry *P*-wave velocity of rocks. *Ultrasonics.* 2007;46(4):341–8.
- Kappelmeyer O, Gérard A, Schloemer W, Ferrandes R, Rummel F, Benderitter Y. European HDR project at Soultz-sous-Forêts: general presentation. *Geotherm Sci Technol.* 1991;2(4):263–89.
- Klinkenberg LJ. The permeability of porous media to liquids and gases. In: *Drilling and production practice.* Washington D.C: American Petroleum Institute; 1941.
- Ledéser B, Joffre J, Amblès A, Sardini P, Genter A, Meunier A. Organic matter in the Soultz HDR granitic thermal exchanger (France): natural tracer of fluid circulations between the basement and its sedimentary cover. *J Volcanol Geotherm Res.* 1996;70(3–4):235–53.
- Ledéser B, Hebert R, Genter A, Bartier D, Clauer N, Grall C. Fractures, hydrothermal alterations and permeability in the Soultz enhanced geothermal system. *C R Geosci.* 2010;342(7):607–15.
- Lengliné O, Boubacar M, Schmittbuhl J. Seismicity related to the hydraulic stimulation of GRT1, Rittershoffen, France. *Geophys J Int.* 2017;208(3):1704–15.
- Louis L, David C, Robion P. Comparison of the anisotropic behaviour of undeformed sandstones under dry and saturated conditions. *Tectonophysics.* 2003;370(1):193–212.
- Louis L, David C, Metz V, Robion P, Menendez B, Kissel C. Microstructural control on the anisotropy of elastic and transport properties in undeformed sandstones. *Int J Rock Mech Min Sci.* 2005;42(7):911–23.
- Louis L, Baud P, Tf Wong. Microstructural inhomogeneity and mechanical anisotropy associated with bedding in Rothbach sandstone. *Pure Appl Geophys.* 2009;166(5):1063–87.
- Magnenet V, Fond C, Genter A, Schmittbuhl J. Two-dimensional THM modelling of the large scale natural hydrothermal circulation at Soultz-sous-Forêts. *Geotherm Energy.* 2014;2(1):17.
- Martys NS, Torquato S, Bentz DP. Universal scaling of fluid permeability for sphere packings. *Phys Rev E.* 1994;50(1):403.
- McCann T (ed) *The Geology of Central Europe Volume 2: Mesozoic and Cenozoic.* Geological Society of London ISBN: 978-1-86239-264-9. 2008.
- McIntosh RM, Sharp JH, Wilburn FW. The thermal decomposition of dolomite. *Thermochim Acta.* 1990;165(2):281–96.
- Moriya H, Niitsuma H, Baria R. Multiplet-clustering analysis reveals structural details within the seismic cloud at the Soultz geothermal field, France. *Bull Seismol Soc Am.* 2003;93(4):1606–20.
- Nelson PH. Permeability-porosity relationships in sedimentary rocks. *Log Anal.* 1994;35(03):38.
- Nollet S, Koerner T, Kramm U, Hilgers C. Precipitation of fracture fillings and cements in the Buntsandstein (NW Germany). *Geofluids.* 2009;9(4):373–85.
- Orywall P, Drüppel K, Kuhn D, Kohl T, Zimmermann M, Eiche E. Flow-through experiments on the interaction of sandstone with Ba-rich fluids at geothermal conditions. *Geotherm Energy.* 2017;5(1):20.
- Place J, Diraison M, Naville C, Géraud Y, Schaming M, Dezayes C. Decoupling of deformation in the Upper Rhine Graben sediments. Seismic reflection and diffraction on 3-component Vertical Seismic Profiling (Soultz-sous-Forêts area). *CR Geosci.* 2010;342(7):575–86.
- Pribnow D, Schellschmidt R. Thermal tracking of upper crustal fluid flow in the Rhine Graben. *Geophys Res Lett.* 2000;27(13):1957–60.
- Robion P, David C, Dautriat J, Colombier JC, Zinsmeister L, Collin PY. Pore fabric geometry inferred from magnetic and acoustic anisotropies in rocks with various mineralogy, permeability and porosity. *Tectonophysics.* 2014;629:109–22.
- Sausse J, Fourar M, Genter A. Permeability and alteration within the Soultz granite inferred from geophysical and flow log analysis. *Geothermics.* 2006;35(5):544–60.
- Sausse J, Dezayes C, Dorbath L, Genter A, Place J. 3D model of fracture zones at Soultz-sous-Forêts based on geological data, image logs, induced microseismicity and vertical seismic profiles. *CR Geosci.* 2010;342(7):531–45.
- Shapiro SA, Audigane P, Royer JJ. Large-scale in situ permeability tensor of rocks from induced microseismicity. *Geophys J Int.* 1999;137(1):207–13.
- Smith P, Davis SJ, Creutzig F, Fuss S, Minx J, Gabrielle B, Kato E, Jackson RB, Cowie A, Kriegler E, Van Vuuren DP, Rogelj J, Ciais P, Milne J, Canadell JG, McCollum D, Peters G, Andrew R, Krey V, Shrestha G, Friedlingstein P, Gasser T, Grüber A, Heidug WK, Jonas M, Jones CD, Kraxner F, Littleton E, Lowe J, Moreira JR, Nakicenovic N, Obersteiner M, Patwardhan A, Rogner M, Rubin E, Sharifi A, Torvanger A, Yamagata Y, Edmonds J, Yongsung C. Biophysical and economic limits to negative CO₂ emissions. *Nat Clim Change.* 2016;6(1):42–50.
- Stober I, Bucher K. Hydraulic and hydrochemical properties of deep sedimentary reservoirs of the Upper Rhine Graben, Europe. *Geofluids.* 2015;15(3):464–82.
- Tanikawa W, Shimamoto T. Klinkenberg effect for gas permeability and its comparison to water permeability for porous sedimentary rocks. *Hydrol Earth Syst Sci Dis.* 2006;3(4):1315–38.
- Tanikawa W, Shimamoto T. Comparison of Klinkenberg-corrected gas permeability and water permeability in sedimentary rocks. *Int J Rock Mech Min Sci.* 2009;46(2):229–38.
- Tembe S, Vajdova V, Baud P, Zhu W, Tf Wong. A new methodology to delineate the compactive yield cap of two porous sandstones under undrained condition. *Mech Mater.* 2007;39(5):513–23.

- Ufer K, Kleeberg R, Bergmann J, Dohrmann R. Rietveld refinement of disordered illite-smectite mixed-layer structures by a recursive algorithm. I: one-dimensional patterns. *Clays Clay Miner.* 2012a;60(5):507–34.
- Ufer K, Kleeberg R, Bergmann J, Dohrmann R. Rietveld refinement of disordered illite-smectite mixed-layer structures by a recursive algorithm. II: powder-pattern refinement and quantitative phase analysis. *Clays Clay Miner.* 2012b;60(5):535–52.
- Vernoux JF, Genter A, Razin P, Vinchon C. Geological and petrophysical parameters of a deep fractured sandstone formation as applied to geothermal exploitation. *BRGM Rep.* 1995;38622:70.
- Vidal J, Genter A, Schmittbuhl J. How do permeable fractures in the Triassic sediments of Northern Alsace characterize the top of hydrothermal convective cells? Evidence from Soultz geothermal boreholes (France). *Geotherm Energy.* 2015;3(1):8.
- Vidal J, Genter A, Chopin F. Permeable fracture zones in the hard rocks of the geothermal reservoir at Rittershoffen, France. *J Geophys Res.* 2017. <https://doi.org/10.1002/2017JB014331>.
- Vogt C, Marquart G, Kosack C, Wolf A, Clauser C (2012a) Estimating the permeability distribution and its uncertainty at the EGS demonstration reservoir Soultz-sous-Forêts using the ensemble Kalman filter. *Water Resour Res.* 48(8). <https://doi.org/10.1029/2011WR011673>.
- Vogt C, Kosack C, Marquart G. Stochastic inversion of the tracer experiment of the enhanced geothermal system demonstration reservoir in Soultz-sous-Forêts—Revealing pathways and estimating permeability distribution. *Geothermics.* 2012b;42:1–12.
- Wadsworth FB, Vasseur J, Scheu B, Kendrick JE, Lavallée Y, Dingwell DB. Universal scaling of fluid permeability during volcanic welding and sediment diagenesis. *Geology.* 2016;44(3):219–22.
- Wong Tf, David C, Zhu W. The transition from brittle faulting to cataclastic flow in porous sandstones: mechanical deformation. *J Geophys Res.* 1997;102(B2):3009–25.
- Zamora M, Poirier JP. Experimental study of acoustic anisotropy and birefringence in dry and saturated Fontainebleau sandstone. *Geophysics.* 1990;55(11):1455–65.
- Zang A, Wagner CF, Dresen G. Acoustic emission, microstructure, and damage model of dry and wet sandstone stressed to failure. *J Geophys Res.* 1996;101(B8):17507–21.
- Zhu W, Montesi LG, Tf Wong. Shear-enhanced compaction and permeability reduction: triaxial extension tests on porous sandstone. *Mech Mater.* 1997;25(3):199–214.
- Zhu W, Wong TF. The transition from brittle faulting to cataclastic flow: permeability evolution. *J Geophys Res.* 1997;102(B2):3027–41.

Submit your manuscript to a SpringerOpen[®] journal and benefit from:

- ▶ Convenient online submission
- ▶ Rigorous peer review
- ▶ Open access: articles freely available online
- ▶ High visibility within the field
- ▶ Retaining the copyright to your article

Submit your next manuscript at ▶ springeropen.com
